

Geophysical applications of nuclear resonant spectroscopy

Wolfgang Sturhahn and Jennifer M. Jackson*

17th August 2007

Advanced Photon Source, Argonne National Laboratory, 9700 South Cass Ave, Argonne, IL 60439, USA; *Seismological Laboratory, Division of Geological and Planetary Sciences, California Institute of Technology, Pasadena, CA 91125, USA

GSA Monograph, Eiji Ohtani, editor (in press)

Abstract

We summarize recent developments of nuclear resonant spectroscopy methods like nuclear resonant inelastic x-ray scattering and synchrotron Mössbauer spectroscopy, and their use for the geophysical sciences. The inelastic method provides specific vibrational information, e.g., the phonon density of states, and in combination with compression data permits the determination of sound velocities and Grüneisen parameters under high pressure and high temperature. The Mössbauer method gives hyperfine interactions between the resonant nucleus and electronic environment like isomer shifts, quadrupole splittings, and magnetic fields, which provide important information on valence, spin state, and magnetic ordering. Both methods use a nuclear resonant isotope as a probe and can be applied under high pressure and high temperature. The physical mechanism of nuclear resonant scattering and the specifics in applications to Earth materials will be discussed with reference to several high-pressure studies on iron-bearing compounds.

1 Introduction

The chemical composition, the elastic and transport properties, and the thermodynamic parameters of materials identified or expected in Earth's deep interior are of general importance to geochemical modeling [Tolstikhin and Hofmann 2005 and Coltice and Ricard 1999], geodynamic simulation [Nakagawa and Tackley 2005], and interpretation of seismic wave observations [add to seismic: Birch 1952; Mattern et al. 2005] (*Kellogg et al.*, 1999; *van der Hilst and Kàrason*, 1999; *Trampert et al.*, 2004; *Ishii and Tromp*, 1999; ?). Inferences of the mineralogy and chemical composition of Earth's deep interior must depend on comparing accurate laboratory-derived properties of candidate phases with geophysical observations, because our ability to directly sample the deep Earth is severely limited. Typically, models of the deep Earth have been made by extrapolating mineral properties to appropriate pressure-temperature (P-T) conditions and comparing them with seismologically determined properties, such as sound velocities and density. Many extrapolations use either low P-T data, infer that the chemically complex minerals behave the same as their Mg-end-members, use analogue materials, and/or neglect the behavior of the shear properties (due in part to lack of experimental data). Although useful, these

assumptions may not accurately reflect the behavior or chemistries of the actual components in the deep Earth. Recent advances in experimental methods and theoretical calculations show that elements such as iron, aluminum, and calcium have appreciable effects on the shear properties of lower mantle silicates and oxides [could add Jackson et al. 2005] (*Jacobsen et al.*, 2002; *Kung et al.*, 2002; *Karki and Crain*, 1998; *Kiefer et al.*, 2002; ?; *Jacobsen et al.*, 2004) and therefore alter our interpretations of geophysical observations. The addition of light elements such as silicon, oxygen, sulfur, and hydrogen to iron also have significant effects on the shear properties (*Machova and Kadeckova*, 1977; *Struzhkin et al.*, 2001; *Lin et al.*, 2003, 2004a; ?; *Jacobsen et al.*, 2004). Several experiments have been performed to understand the crystal chemistry of these complex systems (*Irifune*, 1994; *Kesson et al.*, 1995; *Wood and Rubie*, 1996; *Hirose et al.*, 1999; *Frost and Langenhorst*, 2002) and show that even though most of the iron in mantle materials is divalent (Fe^{2+}) a significant amount of trivalent iron (Fe^{3+}) was determined for aluminum-bearing $(\text{Mg,Fe})\text{SiO}_3$ -perovskite (*McCammon*, 1997). Related to these effects are the possible occurrences of high-spin to low-spin crossovers in the iron component of lower mantle phases (*Badro et al.*, 2003, 2004; *Li et al.*, 2004; *Jackson et al.*, 2005; *Lin et al.*, 2005). Theoretical predictions indicate that material properties influenced by the spin state of iron change smoothly along the geotherm (*Sturhahn et al.*, 2005) but owing to the possible significance of these electronic changes to our interpretation of geophysical observations, more experiments need to be done to clarify the nature of these changes at typical P–T conditions. Even less is known about the recently discovered post-perovskite phase (e.g., *Murakami et al.*, 2004). The effect of iron (*Mao et al.*, 2004) and aluminum (*Akber-Knutson et al.*, 2005) on the perovskite to post-perovskite transition pressure has been studied experimentally and theoretically, respectively, but still little is known about the physical and chemical properties of post-perovskite. It is necessary to study the elastic parameters (especially the shear properties) of deep Earth materials, the valence state of iron in these materials, and the elemental partitioning under appropriate P–T conditions to constrain the chemistry and composition of this region. Many of these unknowns could be determined using nuclear resonant scattering methods under simultaneous high-pressure and high-temperature conditions.

The environmental conditions of planetary interiors often require challenging studies of materials under pressures exceeding 100 GPa and high temperatures. The combination of synchrotron radiation techniques with high-pressure studies has been very successful over the last decades to address these challenges. In particular, the brightness of 3rd-generation synchrotron radiation facilities has permitted scientists to reach ever higher pressures with increasingly small samples. Focusing optics has been refined to concentrate a significant portion of the x-ray beam into an area of less than $10 \times 10 \mu\text{m}^2$ size, and, in combination with efficient high-resolution monochromators, the application of inelastic x-ray scattering and nuclear resonant scattering methods to high-pressure problems has become feasible (see the overview by *Hemley et al.*, 2005). Among nuclear resonant scattering techniques, practical importance has been achieved by nuclear resonant inelastic x-ray scattering (NRIXS) for the study of lattice dynamics and by synchrotron Mössbauer spectroscopy (SMS) for the study of magnetism and valence states. In brief, SMS includes scattering processes that occur recoilless, i.e., without participation of lattice vibrations, whereas NRIXS uses the possibility of simultaneous excitation of nuclear resonance and lattice vibrations. A comprehensive overview of the field has been given in a collection of review articles (*Gerdau and de Waard*, 1999), and also in more recent reviews on nuclear resonant spectroscopy (*Alp et al.*, 2001; *Sturhahn*, 2004; *Scheidt et al.*, 2005). The NRIXS and SMS methods can be applied to materials that contain a nuclear resonant isotope – ^{57}Fe , for example, for geophysical applications.

In this paper, we will first briefly explain the basics on nuclear resonances, as well as some experimental aspects of NRIXS and SMS measurements. Following the experimental section, we discuss the relevant geophysical parameters that can be determined using nuclear resonant scattering, such as a detailed discussion of sound velocities, Grüneisen parameters, temperature, magnetism, valence and spin state.

2 Basics on nuclear resonances

Standard text books on experimental techniques with synchrotron radiation discuss mechanisms that are based on the scattering of x rays by electronic charge and spin. An argument from classical electrodynamics usually provides the justification to ignore the nuclear charge. The Thomson-scattering cross section for electromagnetic radiation by a point charge q with mass m is given by

$$\sigma_T = \frac{8\pi}{3} \left(\frac{q^2}{mc^2} \right)^2 . \quad (1)$$

The scattering strength of the nucleus compared to the electron shell is then reduced by a factor $(Z m/M)^2 \approx 10^{-7}$, where m, M are the masses of the electron and nucleus, and Z is the atomic number. In this long-wavelength limit, which is justified for x rays, the nuclear charge scattering is reduced by orders of magnitude because of the large nuclear mass, and it seems completely appropriate to ignore scattering contributions from the nucleus. However, the above argument fails if the time scale of internal nuclear dynamics matches the energy of the x-ray photon, i.e., the nucleus experiences a resonant excitation. The nuclear resonant cross section is then calculated as

$$\sigma_N = \frac{\lambda^2}{2\pi} \frac{1}{1 + \alpha} \frac{2I' + 1}{2I + 1} , \quad (2)$$

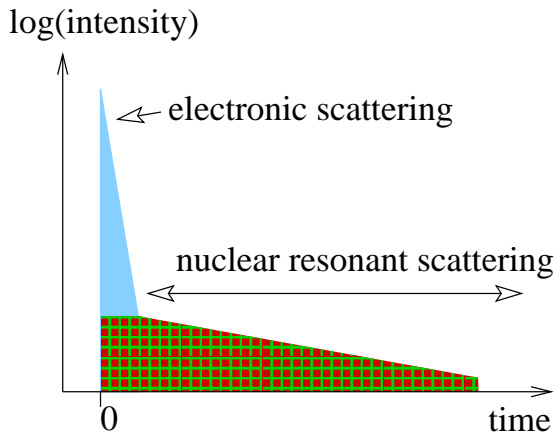


Figure 1: Scattered intensity versus time. At zero time, a SR pulse excites a sample containing a nuclear resonant isotope. Electronic scattering is prompt whereas the response of the resonant nuclei is delayed. Time discrimination is the key to distinguishing nuclear and electronic scattering.

where λ is the wavelength of the resonant x rays, α is the internal conversion coefficient, and I, I' are the spins of the nuclear ground and excited state. The probability that an excited nucleus directly transfers its excess energy to the electron shell followed by expulsion of an inner electron is given by $\alpha/(1 + \alpha)$. Values of α for relevant nuclear transitions range from 1 to 1000. The nuclear resonant cross section can become very large, e.g., the 14.4 keV nuclear transition of ^{57}Fe gives with $\lambda = 86$ pm, $\alpha = 8.6$, $I = 1/2$, $I' = 3/2$ a value of $\sigma_N = 2.56$ Mbarn and a ratio $\sigma_N/\sigma_T \approx 5700$. It should be noted that the photoelectric cross section often exceeds σ_T , but we still observe $\sigma_N/\sigma_{pe} \approx 450$. Even though the nuclear resonant cross section is very large, the energy width of such resonances is very narrow. The weakness of the nuclear coupling to its electronic surroundings and to the electromagnetic field results in a weakly damped resonance of high quality, e.g., the energy width of the ^{57}Fe resonance is only $\Gamma = 4.66$ neV. Such extraordinarily narrow resonances escape traditional x-ray scattering methods because the best energy resolutions of x-ray optics are in the 100- μeV regime (*Toellner et al.*, 2001; ?). A resonant enhancement over a neV scale remains unresolved and unnoticed because even an experiment with bandwidth $\delta E \approx 100 \mu\text{eV}$ would find $\sigma_N \Gamma \ll \sigma_{pe} \delta E$.

Nuclear resonant scattering techniques are nevertheless possible in light of the inverse relationship between lifetime and level width of the nuclear state, $\tau\Gamma = \hbar$. The value of τ determines the time scale on which a sample containing resonant nuclei would respond to an excitation by a synchrotron radiation pulse. Whereas values for τ are in the ns- μs range, the duration of a synchrotron radiation pulse is typically less than 100 ps, and the electronic scattering of x rays occurs typically on the time scale of femtoseconds, virtually immediate compared to nuclear resonant contributions. Detectors with time resolutions of ns or better can exploit this mismatch with a “time-discrimination trick” as illustrated in Figure 1 on page 3, and we understand how nuclear resonant signals are cleanly separated from other scattering contributions. In Figure 2 on page 5, we show the collection of nuclear isotopes that possess resonances below 150 keV. The higher transition energies are less favorable because the intensity of synchrotron radiation sources typically decreases with increasing x-ray energy, and x-ray optics, as well as detectors, become less efficient at higher energies. The time resolution of x-ray detectors (presently around 1 ns) limits the feasibility of short-lived isotopes, whereas very long lifetimes lead to low signal rates and to difficulties with the storage ring operations.

3 Experimental Methods

The pioneering experimental work on nuclear resonant scattering with synchrotron radiation (*Gerdau et al.*, 1985) strongly suggested to utilize new time-resolved techniques instead of the energy-resolved measurements of conventional Mössbauer spectroscopy. This novel approach resulted from the particular property of synchrotron radiation, which is emitted as a sequence of very short x-ray pulses of typically less than 100 ps duration. The analysis of the time-decay pattern of x-rays scattered off or transmitted through samples containing a suitable nuclear-resonant isotope is equivalent to an energy spectroscopy in the μeV to neV (GHz to THz) range. The measurement and analysis of such time spectra constitutes the main part of the SMS method. During the last decade, we experienced the refinement of the SMS technique and its application in the area of high-pressure research (*Nasu*, 1994, 1998; *Zhang et al.*, 1999; *Pleines et al.*, 1999; *Lübberts et al.*, 1999b; *Lin et al.*, 2004a; *Barla et al.*, 2004b,a; *Jackson et al.*, 2005; *Barla et al.*, 2005b,a).

Conventional Mössbauer spectroscopy as well as SMS are based on the often appreciable probability that the resonant nuclei absorb x rays without participation of lattice vibrations, i.e.,

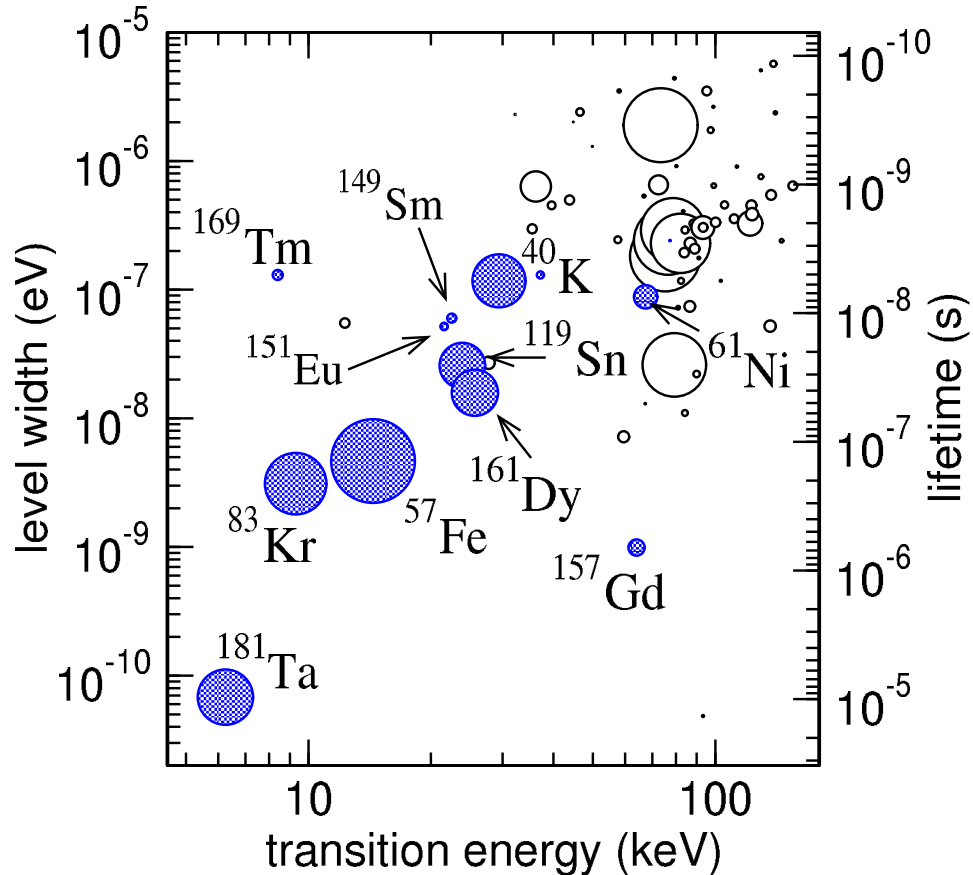


Figure 2: Level widths and lifetimes of nuclear resonances below 150keV. The symbol size is proportional to the nuclear resonant cross section. Isotopes that have been used in NRS experiments are identified.

recoilless. The exclusion of the details of the phonon spectrum from the absorption process leads to the extremely high resolving power of these methods. However, theoretical calculations predicted the exciting opportunity to observe the phonon density of states (DOS) via nuclear resonant excitation (*Visscher, 1960; Singwi and Sjölander, 1960*). Demonstration experiments using strong radioactive sources that were tuned by large Doppler-shifts (*Weiss and Langhoff, 1979; Endres et al., 1981*) were plagued by practical limitations caused by the notoriously small inelastic absorption cross section and overwhelmingly large background signals. Only recently the idea of using nuclear resonances to observe phonon excitations was revived in SR experiments (*Seto et al., 1995; Sturhahn et al., 1995; Chumakov et al., 1995*), and the extraction of the phonon DOS was demonstrated (*Sturhahn et al., 1995*). The use of pulsed synchrotron radiation and a time-discrimination technique circumvented the background problem, and the new NRIXS method started to produce unique results.

The phonon DOS is an important quantity to describe the low-energy collective states of solids and is used to calculate thermodynamic properties related to lattice vibrations. Experimentally the phonon DOS is often obtained indirectly, e.g., by calculation from the phonon dispersion relations measured on single crystals using inelastic neutron scattering. The NRIXS technique provides direct access to the partial and projected phonon DOS of the resonant isotope only (*Kohn et al., 1998; Sturhahn and Kohn, 1999*). The apparent disadvantage to be restricted to

vibrational information from few nuclear resonant isotopes has in turn led to several unique applications. ^{57}Fe is the most suitable nuclear resonant isotope (Figure 2 on page 5), and iron-containing materials, molecules, and proteins are of tremendous interest in geophysics, thin-film research, and biophysics. NRIXS signals originate from particular resonant nuclei only, and this complete isotope selectivity is truly unique among techniques for the study of lattice vibrations. For example, materials surrounding the sample that do not contain resonant nuclei produce no unwanted background, and this feature permitted high-pressure experiments under extreme pressure-temperature conditions that were impossible before (*Lübbbers et al.*, 2000a; *Mao et al.*, 2001; *Struzhkin et al.*, 2001; *Lin et al.*, 2003, 2004a,b; ?; *Shen et al.*, 2004; ?; *Papandrew et al.*, 2004; *Kobayashi et al.*, 2004; *Zhao et al.*, 2004). Details on the scattering mechanisms and methodology for NRIXS and SMS have been given elsewhere (*Chumakov and Sturhahn*, 1999; *Sturhahn*, 2004).

A schematic of the typical NRS experimental setup that can be found at third-generation SR facilities is shown in Figure 3 on page 6. The x-ray source consists of electron bunches that are orbiting in the storage ring and periodically pass through an undulator. The x-rays are monochromatized in two steps using a premonochromator and a high-resolution monochromator to an energy bandwidth of about 1 meV (*Toellner*, 2000).

3.1 NRIXS

For NRIXS measurements, the energy bandwidth of the incident x rays determines the resolution of the phonon spectra of the samples. The high-resolution monochromator is tuned around the nuclear transition energy, and the x rays excite the resonant nuclei in the sample. The incoherently re-emitted radiation is observed with an avalanche photo diode detector that is placed as close as possible to the sample but away from any strong coherent scattering directions (Figure 3 on page 6). The integrated delayed counting rate is recorded. The NRIXS method directly provides the Fourier-transformed self-intermediate scattering function

$$S(\mathbf{k}, E) = \frac{1}{2\pi\hbar} \int \langle e^{i\mathbf{k}\hat{\mathbf{r}}(t)} e^{-i\mathbf{k}\hat{\mathbf{r}}(0)} \rangle e^{iEt/\hbar} dt, \quad (3)$$

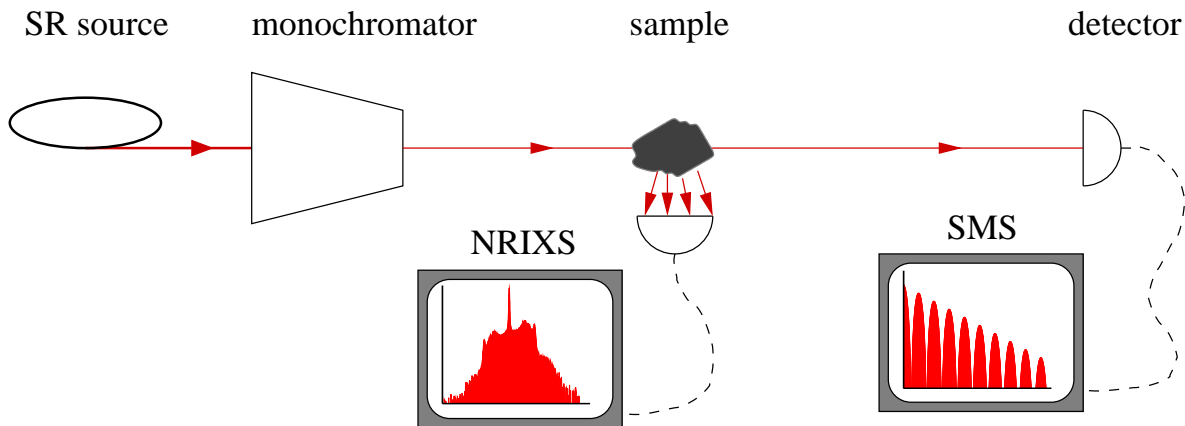


Figure 3: Experimental setup for NRIXS (inelastic incoherent scattering) and SMS (elastic coherent forward-directed scattering). For high-pressure applications, the sample is mounted inside a diamond anvil cell, and focusing mirrors are installed after the monochromator.

where $2\pi\hbar$ is Planck's constant, \mathbf{k} is the wave vector of the x rays incident on the sample, and $\hat{\mathbf{r}}(t)$ is the displacement operator of the resonant nucleus (*Sturhahn and Kohn, 1999; Sturhahn, 2004*). The quasi-harmonic model of lattice vibrations is then used to extract the partial (due to information about motions of the resonant nuclei only) and projected (due to a potential angular dependence on \mathbf{k}) phonon DOS from $S(\mathbf{k}, E)$ (*Sturhahn et al., 1995; Kohn et al., 1998; Hu et al., 1999; Chumakov and Sturhahn, 1999; Sturhahn, 2000, 2004*). Typical acquisition times for a NRIXS spectrum range between one hour for iron-rich samples under ambient conditions and days for dilute samples under very high pressures. The evaluation of the measured NRIXS spectra can be performed using the PHOENIX software (*Sturhahn, 2000*).

3.1.1 The quasi-harmonic model

The vibrations in a solid are determined by the interatomic potential which is harmonic in lowest order of the displacement of the atoms from their equilibrium positions. If higher order terms in the interatomic potential are neglected a solid with N atoms shows $3N - 3$ independent collective vibration modes also known as phonons. The equations of motion can be solved exactly and the self-intermediate scattering function can be calculated for the thermalized ensemble (*Sturhahn and Kohn, 1999*) with the result

$$\begin{aligned}
S(\mathbf{k}, E) &= f(\mathbf{k})\delta(E) + \sum_{n=1}^{\infty} S_n(\mathbf{k}, E) \\
S_1(\mathbf{k}, E) &= f(\mathbf{k}) \frac{E_R}{E(1 - \exp[-\beta E])} g(\mathbf{k}, |E|) \\
S_n(\mathbf{k}, E) &= \frac{1}{nf(\mathbf{k})} \int S_{n-1}(\mathbf{k}, E') S_1(\mathbf{k}, E - E') dE' \\
f(\mathbf{k}) &= \exp \left[- \int \frac{E_R}{E} \coth\left(\frac{\beta E}{2}\right) g(\mathbf{k}, E) dE \right].
\end{aligned} \tag{4}$$

In this expression, $f(\mathbf{k})$ is the probability for recoilless absorption of the x rays also known as the Lamb-Mössbauer factor, E_R is the recoil energy, $\beta = 1/(k_B T)$ is the inverse temperature with Boltzmann's constant k_B , and $g(\mathbf{k}, E)$ is the partial and projected phonon DOS. The expansion has a clear physical interpretation: the value of $S_n(\mathbf{k}, E)dE$ gives the probability for the creation/annihilation of n phonons with a total energy between E and $E + dE$. The extraction of the phonon DOS from measured data based on (4) using the Fourier-log inversion method has been described earlier (*Kohn et al., 1998; Hu et al., 1999; Sturhahn, 2000*).

Beyond the very powerful harmonic model, anharmonic interatomic potentials can arise either from very special atomic arrangements (?) or from increasing atomic separation caused by temperature (*Chumakov et al. 1996?*). Most often anharmonic effects are described by perturbations of the harmonic approximation, and the concepts of "phonon life time" and "phonon scattering length" are introduced (book on phonons). In the analysis of the self-intermediate scattering function, we distinguish situations of weak and strong anharmonicity. The former is characterized by renormalization of phonon energies (mode softening) and finite phonon life time but still assume the existence of phonons as such, i.e., the coupling between the renormalized vibrational modes is negligible. The use of (4) is still justified and will provide the renormalized phonon DOS. Situations of strong anharmonicity defy the phonon interpretation because the collective excitations are very different from phonons and renormalization is not

sufficient, e.g., collective excitations in liquids and fast atomic diffusion in solids fall into this category. The quasi-harmonic model assumes the validity of (4) and gives reliable results for cases of weak anharmonicity as explained above.

If a NRIXS spectrum has been measured on a solid at certain P–T conditions the validity of the weak anharmonicity assumption may be of concern, particularly at temperatures close to melting. Several tests which are based on the internal consistency of (4) have been suggested (*Chumakov and Sturhahn, 1999*). The Lamb-Mössbauer factor, the kinetic energy per resonant atom, and the average force constant of the resonant atom can be calculated either as moments of the measured $S(\mathbf{k}, E)$ or from the phonon DOS (*Chumakov and Sturhahn, 1999; Sturhahn and Chumakov, 1999*). In addition, proper normalization and the positiveness of the phonon DOS can be tested.

3.1.2 Directional dependence

The dependence of $S(\mathbf{k}, E)$ on the direction of the incident x rays is implicitly contained in (3) and is expressed via the directional dependence of the phonon DOS. The potential anisotropy of the phonon DOS must not be confused with the elastic anisotropy: the description of the former is given by a symmetric second-rank tensor (*Sturhahn and Kohn, 1999*) whereas the latter requires a symmetric fourth-rank tensor. Therefore, in crystals with cubic symmetry like ambient bcc-iron, the phonon DOS is isotropic, but the elastic anisotropy is large ($C_{11} = 230$ GPa, $C_{12} = 135$ GPa, $C_{44} = 117$ GPa, anisotropy $A = (2C_{44} + C_{12} - C_{11})/C_{11}$ of about 60%). Anisotropic behavior of the phonon DOS has been observed in FeBO₃ (*Chumakov et al. 1997?*) and hcp-iron (*Giefers et al., 2000*), but the anisotropy of the Lamb-Mössbauer factor was reported to be below the detection limits of 3.5% and 0.1%, respectively. Even single crystals of planar organic molecules show only a variation of about 2.5% in the Lamb-Mössbauer factor (*Rai et al., 2002*). The NRIXS spectrum of polycrystalline materials provides an average value $\langle S(\mathbf{k}, E) \rangle$, and we write, neglecting the small variations of the Lamb-Mössbauer factor

$$\begin{aligned} \langle S(\mathbf{k}, E) \rangle &= f\delta(E) + \sum_{n=1}^{\infty} \langle S_n(\mathbf{k}, E) \rangle \\ \langle S_1(\mathbf{k}, E) \rangle &= \frac{f E_R}{E(1 - \exp[-\beta E])} \langle g(\mathbf{k}, |E|) \rangle \\ \langle S_n(\mathbf{k}, E) \rangle &= \frac{1}{nf} \int \langle S_{n-1}(\mathbf{k}, E') S_1(\mathbf{k}, E - E') \rangle dE' \\ f &= \exp \left[- \int \frac{E_R}{E} \coth\left(\frac{\beta E}{2}\right) \langle g(\mathbf{k}, E) \rangle dE \right] . \end{aligned} \quad (5)$$

Unfortunately the averaged higher-order terms cannot be derived from the averaged one-phonon term, and the formal inversion of (5) to obtain $\langle g(\mathbf{k}, E) \rangle$, e.g., with the Fourier-log method, requires further justification. If we use the Fourier-log method nevertheless we would obtain a result for the averaged one-phonon term that will of course deviate somewhat from the correct expression. This deviation is approximately given by

$$-\frac{1}{2f} \int \langle \delta_1(\mathbf{k}, E') \delta_1(\mathbf{k}, E - E') \rangle dE' \quad \text{with } \delta_1(\mathbf{k}, E) = S_1(\mathbf{k}, E) - \langle S_1(\mathbf{k}, E) \rangle .$$

We note that this correction is a two-phonon term and of second order in the integrated anisotropy functions δ_1 . Reported cases of anisotropy (*Chumakov et al. 1997?*)(*Giefers et al.,*

2000) would lead to estimates of much less than 1% for this term. Direct inversion of the measured NRIXS spectrum therefore provides a reliable value of the averaged phonon DOS, unless the material exhibits a large anisotropy and small Lamb-Mössbauer factor (which have yet to be observed).

3.2 SMS

For SMS measurements, the energy bandwidth should be as small as practicably achievable with reasonable efficiency. The high-resolution monochromator is tuned to the nuclear transition energy and kept as stable as possible. X rays that are transmitted through the sample excite the resonant nuclei coherently and are observed with an avalanche photo diode detector that is placed far enough away from the sample to avoid contamination from incoherent scattering. The delayed events are mapped as a function of elapsed time between arrival of a synchrotron radiation pulse and detection of transmitted x-ray photon – this constitutes the time spectrum of the nuclei in the sample.

The delayed transmitted intensity can be expressed in terms of the nuclear contribution to the index of refraction of the sample (*Sturhahn, 2004*)

$$\delta n(E) = \frac{\lambda}{4\pi} \rho \sigma_N f \sum_{mm'} \frac{W_{mm'}}{z_{mm'}(E) - i}, \quad (6)$$

where λ is the x-ray wavelength, ρ is the volume density of resonant nuclei, σ_N is the nuclear resonant cross section, and f is the Lamb-Mössbauer factor. The sum is over all sub-levels of nuclear ground and excited states. The function $z_{mm'} = 2(E_{mm'} - E)/\Gamma$ depends on the energy difference between excited and ground states $E_{mm'}$ and the nuclear level width Γ . The weight of each resonance at $E_{mm'}$ is given by the second-rank tensor $W_{mm'}$. The weights are normalized by $\sum_{mm'} W_{mm'} = 1$. The index of refraction has sharp maxima at energies $E = E_{mm'}$ corresponding to the positions of the nuclear transitions which are determined by the electronic environment of the nucleus. The time spectrum is given by

$$\begin{aligned} \frac{dI}{dt} &= \frac{I_0}{(2\pi\hbar)^2} \left| \int (\exp[ikD\delta n] - 1) e^{-iEt/\hbar} dE \right|^2 \\ &= \frac{I_0}{(2\pi\hbar)^2} \left| \int \left(\exp \left[i \frac{\eta}{2} \sum_{mm'} \frac{W_{mm'}}{z_{mm'}(E) - i} \right] - 1 \right) e^{-iEt/\hbar} dE \right|^2, \end{aligned} \quad (7)$$

where I_0 is the incident intensity corrected by electronic absorption, $k = E/(\hbar c)$ is the wave number, and D is the physical thickness of the sample. The effective thickness $\eta = \rho \sigma_N f D$ is a useful parameter to describe total intensity and the influence of sample thickness on the shape of the time spectra. An effective thickness between 10 and 50 usually provides a good compromise between a distortion of the time spectra for larger values of η and a small total counting rate for smaller values of η . Typical acquisition times for a SMS time spectrum range between minutes for iron-rich samples under ambient conditions and a few hours for dilute samples under high pressures. Measured time spectra can be evaluated with the CONUSS software (*Sturhahn, 2000*). It should be noted that the index of refraction cannot be calculated by a simple Fourier transformation of the time spectrum. This situation has been described as the phase problem of SMS (*Sturhahn, 2001*), and experimental schemes to circumvent this problem have been proposed (*Sturhahn et al., 2004*). At present such schemes would lead to a large increase in data collection time and are not routinely applied in high-pressure experiments.

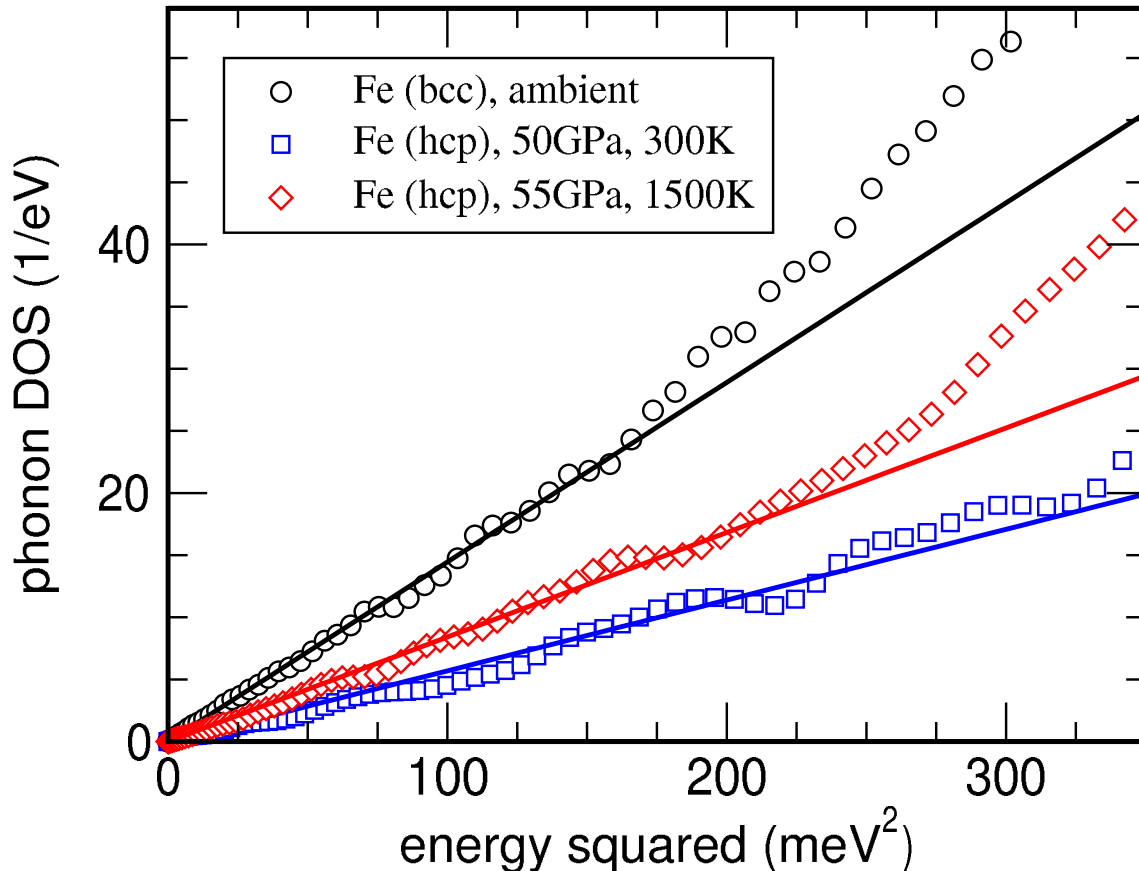


Figure 4: Phonon DOS versus energy squared. The straight lines are fits to the data for energy below about 15 meV. In this energy region, Debye-like behavior is observed. The data are taken from *Sturhahn, 2004* (ambient) and ? (high pressure).

4 Sound Velocities

The starting point for sound velocity measurements is the phonon DOS that is extracted from the NRIXS data. The connection between the phonon DOS and sound velocities may not be immediately obvious. In solids, sound waves and acoustic phonons of wavelengths much larger than inter-atomic distances describe the same physical phenomenon. The “phonon-picture” emphasizes microscopic properties, like inter-atomic force constants, whereas the macroscopic descriptors like elastic moduli and density dominate the understanding of the “sound-wave picture.” The energy of an acoustic phonon of mode s with a long wavelength λ that propagates in the direction \mathbf{q} is given by $E_s = \hbar v_s(\mathbf{q})/\lambda$, where \hbar is Planck’s constant and $v_s(\mathbf{q})$ is the sound velocity. The number of phonon states in momentum space is then $dN_s = V \int k_s^2 dk_s d\Omega_q$, where $k_s = E_s/(\hbar v_s)$, V is a normalization volume, and the integration is performed over all directions \mathbf{q} . The linear phonon dispersion leads to a Debye-like phonon DOS

$$D(E) = \sum_s \frac{dN_s}{dE} = \frac{VE^2}{\hbar^3} \sum_s \int \frac{1}{v_s^3(\mathbf{q})} d\Omega_q . \quad (8)$$

This relationship is exact for small energies (long phonon wavelengths) and has been experimentally shown to hold even in the case of a partial phonon DOS of a particular type of atom

in a compound (*Hu et al.*, 2003). Here the previous equation was given in a form suitable for quantitative analysis

$$D(E) = \frac{\tilde{m}}{2\pi^2\hbar^3\rho} \frac{1}{v_D^3} E^2 \quad \text{with} \quad \frac{1}{v_D^3} = \frac{1}{3} \sum_s \int \frac{1}{v_s^3(\mathbf{q})} \frac{d\Omega_q}{4\pi}, \quad (9)$$

where v_D is the Debye sound velocity, ρ is the density of the material, and \tilde{m} is the mass of the nuclear resonant isotope.

4.1 Debye sound velocity

The quantitative description of the low-energy region of the phonon DOS via (9) provides the Debye sound velocity. In Figure 4 on page 10, the low-energy region of the phonon DOS is shown for iron metal under different pressures and temperatures. Fits to the data provide the curvature of the parabola defined by (9), and with the known density one derives Debye sound velocities of 3.49(5) km/s for ambient conditions, 4.54(6) km/s for 50 GPa and 300 K, and 3.98(1) km/s for 55 GPa and 1500 K. In a similar way, Debye sound velocities were obtained for iron metal (*Mao et al.*, 2001), Fe-Ni and Fe-Si alloys (*Lin et al.*, 2003), Fe_{0.9x}O (*Struzhkin et al.*, 2001), Fe₃S (*Lin et al.*, 2004a), FeH_x (?), and FeS (*Kobayashi et al.*, 2004) under high pressure. Very recently the same method was applied to measure the temperature dependence of sound velocities in compressed iron metal (?). In Table 1 on page 12 we compare Debye sound velocities from NRIXS measurements with calculated Debye sound velocities from reported values for the elastic constants. We numerically determined sound velocities from the Christoffel equation [Musgrave 1970] for all crystal directions and applied the averaging procedure of (9) to obtain the Debye sound velocity.

The derivation of Debye sound velocities from the phonon DOS relies on a linear phonon dispersion which will only be accurate in a limited energy range as seen from the deviations apparent in Figure 4 on page 10 for energies above about 15 meV. The energy resolution of the NRIXS method depends on the bandwidth of the x rays incident on the sample and with present monochromator technology reaches about 1 meV. In measured data, we therefore expect the energy region below about 2-3 meV to be obscured by elastic scattering and less reliable for sound-velocity determination. Even though this does not seem to be a problem for the analysis of the data on pure iron that is shown in Figure 4 on page 10, other materials may be more problematic. We will estimate the systematic errors resulting from the use of (9) by an improved, empirical relation for the dispersion of the acoustic phonons. Assume that the phonon energies reach a maximum value of E_{cs} at the Brillouin-zone boundary and that we can describe the phonon energies by $E_s = E_{cs} \sin(hv_s/\lambda E_{cs})$, a relationship used before to extract compressional sound velocities using the IXS method (*Fiquet et al.*, 2001). We then obtain a relationship similar to (9) but with an energy-dependent Debye velocity

$$\frac{1}{v_D^3(E)} = \frac{1}{3} \sum_s \frac{\arcsin^2 \eta_s}{\eta_s^2 \sqrt{1 - \eta_s^2}} \int \frac{1}{v_s^3(\mathbf{q})} \frac{d\Omega_q}{4\pi}, \quad (10)$$

with $\eta_s = E/E_{cs}$. If we use the energy interval $[E_1, E_2]$ for analysis the average Debye sound velocity is given by

$$\frac{1}{\bar{v}_D^3} = \frac{1}{v_D^3(0)} + \frac{1}{3} \sum_s \left\{ \frac{\arcsin^3(E_2/E_{cs}) - \arcsin^3(E_1/E_{cs})}{3(E_2 - E_1)/E_{cs}} - 1 \right\} \int \frac{1}{v_s^3(\mathbf{q})} \frac{d\Omega_q}{4\pi}. \quad (11)$$

The correction term in this expression is positive, and analysis of the measured data by a parabolic fit would provide a smaller Debye sound velocity if the phonon dispersion is nonlinear in the interval $[E_1, E_2]$. For the iron data shown in (9), typical parameters of $E_{cs} = 25$ meV, $E_1 = 3$ meV, and $E_2 = 12$ meV lead to about 4% reduction in the derived Debye sound velocity. This effect can be reduced further by decreasing E_2 even though at present the statistical quality of typical high-pressure NRIXS data would probably require $E_2 \geq 10$ meV.

4.2 Compressional and shear wave velocities

Seismic data of Earth’s interior distinguish between compressional waves and shear waves corresponding to longitudinally and transversely polarized phonons, respectively. The polarization vectors $\mathbf{e}_s(\mathbf{q})$ of the phonons can be used to define average compressional and shear

Table 1: Measured Debye sound velocities of Earth-relevant materials from NRIXS (noted with *) compared with calculated Debye sound velocities from available single-crystal elasticity information. Errors for values from NRIXS include statistical contributions only. All values are for ambient conditions, unless mentioned otherwise.

material	density (g/cm ³)	v_D (m/s)	reference
α -Fe	7.86 [†]	3521±50*	<i>Sturhahn, 2004</i>
α -Fe	7.86 [†]	3519±48*	<i>Hu et al., 2003</i>
α -Fe	7.874	3538	<i>Hearmon, 1984</i>
Fe _{0.85} Si _{0.15}	7.42±0.01	3281±10*	<i>Lin et al., 2003</i>
Fe _{0.91} Si _{0.09}	7.601	3541	<i>Machova and Kadeckova, 1977</i>
Fe _{0.94} Si _{0.06}	7.675	3556	<i>Machova and Kadeckova, 1977</i>
Fe _{0.92} Ni _{0.08}	8.40±0.02	3530±6*	$P = 7.5$ GPa (<i>Lin et al., 2003</i>)
Fe ₃ S	7.05	2902±6*	<i>Lin et al., 2004a</i>
FeS	4.6	2831±10*	$P = 1.5$ GPa, from <i>Kobayashi et al., 2004</i>
Fe _{0.947} O	5.708	2801*	$P = 0.9$ GPa, from <i>Struzhkin et al., 2001</i>
Fe _{0.943} O	5.708	3210	<i>Jackson and Khanna, 1990</i>
Fe _{0.946} O	5.721±0.006	3223±7	<i>Jacobsen et al., 2002</i>
Fe ₂ O ₃	5.254	4597±100*	this study
Fe ₂ O ₃	5.254	4654±100	<i>Liebermann and Schreiber, 1968[‡]</i>

[†] *Weast (1984)*.

*Debye sound velocity from NRIXS data and corrected for natural Fe-enrichment using $\text{Fe}_{(1-x)}\text{R}_x$ and $\frac{v_{\text{natural}}}{v_{\text{enriched}}} = \sqrt{\frac{(1-x)57 + xA_R}{(1-x)56 + xA_R}}$, where A_R represents the atomic mass of the non-enriched portion.

Note that all other Debye sound velocities were calculated from available single-crystal elasticity data (unless mentioned otherwise) using the Christoffel equation and the averaging method outlined in (9).

[‡] polycrystalline sample.

wave velocities v_P and v_S by

$$\frac{1}{v_P^3} = \sum_s \int \frac{[\mathbf{q} \cdot \mathbf{e}_s(\mathbf{q})]^2}{v_s^3(\mathbf{q})} \frac{d\Omega_q}{4\pi} \quad \text{and} \quad \frac{1}{v_S^3} = \frac{1}{2} \sum_s \int \frac{1 - [\mathbf{q} \cdot \mathbf{e}_s(\mathbf{q})]^2}{v_s^3(\mathbf{q})} \frac{d\Omega_q}{4\pi} . \quad (12)$$

The NRIXS method provides the Debye sound velocity which according to (9) and (12) can now be expressed as

$$\frac{3}{v_D^3} = \frac{1}{v_P^3} + \frac{2}{v_S^3} . \quad (13)$$

For isotropic media, v_P and v_S are independent of direction and follow the additional relationship

$$\frac{K_s}{\rho} = v_\phi^2 = v_P^2 - \frac{4}{3}v_S^2 , \quad (14)$$

where K_s and ρ are the adiabatic bulk modulus and density, respectively. (13) and (14) have widely been used to derive compressional and shear wave velocities from NRIXS data with additional knowledge of adiabatic bulk modulus and density. These equations have general solutions

$$v_S = 0.952 v_D - 0.041 v_\phi \quad v_P = 0.908 v_\phi + 0.297 v_D - 0.243 v_D^2/v_\phi , \quad (15)$$

which are accurate to better than 0.1%. A variation of v_ϕ has only a minor effect on the shear wave velocity, i.e., $\delta v_S = -0.041 \delta v_\phi$, whereas $\delta v_P = (0.908 - 0.243 v_D^2/v_\phi^2) \delta v_\phi$ reflects the strong influence of v_ϕ on the value for the compressional wave velocity. The weak effect of v_ϕ on the shear wave velocity determination of FeH_x has been pointed out previously (?). Here we emphasize the generality of this finding, and, as a result, the NRIXS method is particularly suitable to provide precise values for the average shear wave velocity, where the averaging mechanism is defined by (12). In Figure 5 on page 24, we show examples of sound velocities of iron and iron alloys at room temperature. The straight lines are fits to the NRIXS results and suggest the validity of Birch's law (*Birch*, 1952) for v_P and v_S , i.e., $v_{P,S} \propto \rho$. The same linear dependence of v_P and v_S was also found independently in inelastic x-ray scattering studies (?). In addition, recent NRIXS experiments on iron under high pressure and high temperature have demonstrated an explicit temperature dependence of the sound velocities at constant density (?).

It is important to realize that (14) will only hold approximately for elastically anisotropic materials. For example, a calculation using elastic constants of iron metal at ambient conditions ($C_{11} = 230$ GPa, $C_{12} = 135$ GPa, $C_{44} = 117$ GPa, anisotropy $A = (2C_{44} + C_{12} - C_{11})/C_{11}$ of about 60%) shows that the right side of (14) will fall short of its correct value by about 4% when using the average velocities according to (12) and potentially more for materials with larger elastic anisotropy. Nevertheless average shear wave velocities can be determined by NRIXS with great precision and high accuracy. Consider solutions (v_P , v_S) of (13) and (14), where v_D and v_ϕ serve as input parameters. A variation of v_ϕ can then simulate the effects of elastic anisotropy and uncertainty in the bulk modulus. According to (15) uncertainty about the elastic anisotropy will then mainly influence v_P whereas the v_S almost unchanged.

4.3 Compound mixtures

The previous discussion implicitly assumed a homogeneous material under investigation. Even though most experiments may try to prepare and study pure samples, the effect of a mixture of

compounds with different elastic properties on the sound velocity determination is important. For simplicity, we will assume a mixture of only two compounds with concentrations α_1 and $\alpha_2 = 1 - \alpha_1$. The NRIXS spectrum will then be given by $S(E) = \alpha_1 S_1(E) + \alpha_2 S_2(E)$, where $S_j(E)$ are the self-intermediate scattering functions according to (3) for each compound. The extracted phonon DOS is non-linearly related to $S(E)$ and is in general not the linear superposition of the phonon DOS of the two compounds (see the discussion in *Sturhahn and Chumakov, 1999*). If we still assume that the extracted phonon DOS is a linear superposition we will make an error of the order $(f - 1 - f \ln f)/(f \ln f)$, which can be approximated by $3(1 - f)^2/2$ for Lamb-Mössbauer factors close to unity. For example, hcp-iron at 300 K gives $f > 0.83$, and the error would be only a few percent. Under these conditions it is justified to assume a linear superposition of the phonon DOS which leads to the following addition rule for the Debye sound velocities

$$f \rho v_D^{-3} = f_1 \alpha_1 \rho_1 v_{D1}^{-3} + f_2 \alpha_2 \rho_2 v_{D2}^{-3} , \quad (16)$$

where f_j , ρ_j , and v_{Dj} are the Lamb-Mössbauer factors, densities, and Debye sound velocities of the two compounds, and $f = \alpha_1 f_1 + \alpha_2 f_2$. The value on the left side of (16) is obtained from the measured NRIXS spectrum, but in principle the values for the two compounds cannot be measured simultaneously. An important application of (16) is the assessment of effects caused by a contamination of the compound to be studied. In this case, we may set $\rho = \rho_1$ and rewrite (16) as follows

$$\frac{v_D}{v_{D1}} = \left[\frac{\alpha_1 + \alpha_2 \xi}{\alpha_1 + \alpha_2 \xi \eta} \right]^{1/3} , \quad (17)$$

where $\xi = f_1/f_2$ and $\eta = (\rho_2 v_{D1}^3)/(\rho_1 v_{D2}^3)$. In Figure 6 on page 25, we show the ratio of measured and actual Debye sound velocities v_D/v_{D1} for various values of η . The influence of ξ on the results is small, and we chose $\xi = 1$ which is reasonable for most Fe-bearing materials under high pressure. The approximation of (17) for small α_2 reads $v_D/v_{D1} \approx 1 + \alpha_2 \xi (1 - \eta)/3$ which suggests a strong effect for large η . Even small amounts of a dense contaminant with small Debye sound velocity added to a light material with high Debye sound velocity (large values of η) can lead to very different results for the measured value of v_D . For example, a mixture of 0.5% FeO ($\rho_2 = 5.721$ g/cm³, $v_{D2} = 3.221$ km/s) and 99.5% perovskite Mg_{0.9}Fe_{0.1}SiO₃ ($\rho_1 = 4.106$ g/cm³, $v_{D1} = 7.21$ km/s, from *Sinogeikin et al., 2004* for iron-free MgSiO₃) gives $\eta = 15.6$ and $\alpha_2 = 0.16$ which would lead to a measured Debye sound velocity of only $v_D = 4.24$ km/s, a 41% reduction. The method is much more robust in the opposite scenario with small values of η . For example, a mixture of 10% FeO ($\rho_2 = 5.721$ g/cm³, $v_{D2} = 3.221$ km/s) and 90% iron metal ($\rho_1 = 7.86$ g/cm³, $v_{D1} = 3.52$ km/s) gives $\eta = 0.95$ and $\alpha_2 = 0.06$ which leads to a change in the measured Debye sound velocity of only 0.1%.

5 Grüneisen Parameters

The volume and temperature dependence of vibrational modes contains important information about the thermodynamic behavior of condensed matter. A microscopic picture was developed by Grüneisen (*Grüneisen, 1926*) who introduced the isothermal change of the energy ω_l of the vibrational mode l with volume as a characteristic parameter. These mode-specific isothermal Grüneisen parameters are defined by the equation

$$\gamma_l = -\frac{V}{\omega_l} \left(\frac{\partial \omega_l}{\partial V} \right)_T . \quad (18)$$

In principle, there are $3N$ possible different values for the γ_l if N is the number of atoms in the material, and the independent determination of all these parameters is experimentally not feasible. However, the volume dependence of the phonon DOS can be determined by NRIXS. Several types of Grüneisen parameters have been introduced and are used in the literature (see e.g. ?). In particular, the Debye-Grüneisen parameter given by

$$\gamma_D = \frac{1}{3} + \frac{\rho}{v_D} \left(\frac{\partial v_D}{\partial \rho} \right)_T \quad (19)$$

can be extracted from the measured Debye sound velocities v_D . An ansatz of the type $\gamma_D = \gamma_{D0}(\rho_0/\rho)^q$ (*Anderson, 1979*) permits us to integrate the previous equation and leads to the following functional description

$$v_D = v_{D0} \zeta^{1/3} \exp \left(-\frac{\gamma_{D0}}{q} (\zeta^q - 1) \right) , \quad (20)$$

where $\zeta = \rho_0/\rho$. We used (20) to derive values for γ_{D0} and q with density-dependent Debye sound velocities obtained from published NRIXS data on bcc-Fe and hcp-Fe (*Mao et al., 2001*) as well as $\text{Fe}_{0.92}\text{Ni}_{0.08}$ and $\text{Fe}_{0.85}\text{Si}_{0.15}$ (*Lin et al., 2003*). The best agreement was achieved with $\gamma_{D0} = 1.9$ and $q = 1.71$ for bcc-iron, $\gamma_{D0} = 2.36$ and $q = 1.67$ for hcp-iron, $\gamma_{D0} = 1.67$ and $q = 1.1$ for $\text{Fe}_{0.92}\text{Ni}_{0.08}$, $\gamma_{D0} = 2.01$ and $q = 1.13$ for $\text{Fe}_{0.85}\text{Si}_{0.15}$. These Debye-Grüneisen parameters and previously published experimental values on hcp-Fe versus the reduced density ρ/ρ_0 are displayed in Figure 7 on page 26. Previous NRIXS studies provided $\gamma_{D0} = 2.0$ (bcc-Fe) and $\gamma_{D0} = 1.8$ (hcp-Fe in the pressure range below 40 GPa) but assumed $q = 0$ (*Giefers et al., 2000*).

6 Temperature

The NRIXS raw data has a very fundamental property which is independent of the material under investigation: the spectra follow a detailed balance principle (*Sturhahn and Kohn, 1999*). If the NRIXS data are given by $I(E)$ with $E = 0$ as the exact nuclear transition energy, we can write

$$I(-E) = e^{-\beta E} I(E) , \quad (21)$$

where $\beta = 1/(k_B T)$ is the inverse temperature, and k_B is Boltzmann's constant. The above relation permits us to determine the temperature of the sample from the spectral intensity ratios of phonon creation ($E > 0$) and annihilation ($E < 0$) parts. Recently, this method has been applied to determine the temperature of heated samples of iron under pressures up to 29 GPa (*Shen et al., 2004*). A comparison of the temperature from the NRIXS data with a temperature obtained by a fit of the thermal radiation spectra to the Planck radiation function up to 1700 K and 58 GPa confirmed independently the validity of temperatures determined from the spectroradiometric method in laser-heated diamond cell experiments (*Lin et al., 2004b*). In Figure 8 on page 27, we illustrate the effect of temperature on NRIXS data by introducing a thermal asymmetry function defined by

$$A = \frac{I(E) - I(-E)}{I(E) + I(-E)} . \quad (22)$$

The detailed balance principle predicts the thermal asymmetry to behave as $A = \tanh(\beta E/2)$. This function was fitted to the data in the region between 5 meV and 50 meV with only

temperature as an adjustable parameter. The central part was excluded to avoid the influence of the elastic peak. At large energies the statistical accuracy of the data points decreases rapidly. A detailed analysis of error sources related to temperature determination using this method has been given previously (*Shen et al.*, 2004). In Figure 9 on page 28, we show temperatures determined with the spectroradiometric method and from NRIXS spectra on iron in a diamond anvil cell (*Lin et al.*, 2004b). The spectroradiometric temperatures have been averaged over the collection time of the corresponding NRIXS spectra of typically 8 hours.

7 Magnetism

Magnetic ordering in a material causes a characteristic Zeeman splitting of the nuclear levels of the resonant isotope. According to (6) and (7) the SMS time spectrum carries the signature of such a magnetic splitting. The SMS method has been used to investigate magnetism under high pressure using the ^{57}Fe isotope (*Nasu*, 1998; *Lübbbers et al.*, 1999a,b, 2000b; *Rupprecht et al.*, 2000; *Wortmann et al.*, 2002; *Lin et al.*, 2004a; ?) , the ^{151}Eu isotope (*Lübbbers et al.*, 1999a; *Lengsdorf et al.*, 2004), the ^{119}Sn isotope (*Barla et al.*, 2005a), and the ^{149}Sm isotope (*Barla et al.*, 2004b,a, 2005b). Geophysical applications of the SMS method examined the pressure dependence of magnetism in materials like Fe_3S (*Lin et al.*, 2004a) or FeH_x (?). Fe_3S is the most iron-rich sulfide known to date and may be an important component in the iron-sulfur system at high pressures (??). In Figure 10 on page 29, we show representative time spectra and the magnetic hyperfine fields derived from the time spectra of the SMS method together with normalized sound velocities (*Lin et al.*, 2004a). The low-pressure magnetic phase contains two sites with different magnetic hyperfine fields. A collapse of the magnetic order occurs around 21 GPa, and simultaneous SMS and NRIXS experiments showed that the magnetic to non-magnetic transition significantly affects the elastic, thermodynamic, and vibrational properties of Fe_3S (*Lin et al.*, 2004a).

8 Valence and spin state

Most of the minerals and polymorphs expected in Earth’s interior are believed to incorporate low concentrations of Fe^{2+} and/or Fe^{3+} of about 10 atomic% or less. They are not expected to be magnetically ordered in Earth’s lower mantle because of the low Fe content and the elevated temperatures. However, valence and spin state of the Fe in minerals may still be relevant with respect to density, iron partitioning, partial melting, radiative thermal conductivity, and compositional layering (*Shannon and Prewitt*, 1969; *Gaffney and Anderson*, 1973; *Sherman*, 1988, 1991; *Sherman and Jansen*, 1995; *Badro et al.*, 2003, 2004; *Li et al.*, 2004). The SMS method provides quadrupole splittings and isomer shifts similarly to traditional Mössbauer spectroscopy but the high brilliance of the synchrotron radiation reduces the data collection times tremendously, allows easier access for high-pressure studies, and reduces pressure gradients in the observed data (*Sturhahn et al.*, 1998; *Lübbbers et al.*, 1999b; *Sturhahn*, 2004). The assignment of a set of parameter values to valence and spin state is usually based on a fingerprinting scheme (*Bancroft et al.*, 1967).

Traditional Mössbauer spectroscopy had been used previously to study ferro-magnesium silicate perovskite (hereafter referred to as Pv) and Al-bearing Pv under ambient pressure (*McCammon*, 1997). Recently the SMS method has been applied to Pv using compositions $\text{Mg}_{1-y}\text{Fe}_y\text{SiO}_3$ with $y = 0.05$ and $y = 0.1$ up to 120 GPa at room temperature (*Jackson et al.*,

2005). In Figure 11 on page 30, we show the pressure dependence of the quadrupole splittings of the three Fe sites in Pv. The increase of the splitting was explained by the compression of the perovskite lattice. A change of the pressure dependence of the isomer shift between Fe^{2+} and Fe^{3+} around 70 GPa possibly indicates a change in the Fe^{3+} spin state of (*Jackson et al.*, 2005). X-ray emission spectroscopy has also been applied to probe the spin state of Fe in Pv (*Badro et al.*, 2004; *Li et al.*, 2004), Al-bearing Pv (*Li et al.*, 2004), and (Mg,Fe)O ferropericlase (*Badro et al.*, 2003; *Lin et al.*, 2005). In contrast to x-ray emission spectroscopy, SMS can distinguish valences in addition to the spin states of Fe. Specifically, SMS data provide us with different Fe sites characterized by isomer shift and quadrupole splitting.

9 Conclusion

We introduced two particular nuclear resonant scattering techniques that are applied to a variety of problems in condensed-matter physics, material science, geophysics, biophysics, and chemistry. In this contribution, we focused on the geophysical applications. The NRIXS and SMS methods have prospered with the commissioning of third-generation synchrotron radiation sources. We expect even greater potential when the brilliance of these sources will be further increased by optimization of undulator technology or operating parameters of the storage ring. If fourth-generation sources (x-ray lasers) become a reality at sub-Ångström wavelengths, orders of magnitude increases in spectral flux density could lead to tremendous opportunities for the “flux-hungry” nuclear resonant and inelastic x-ray scattering techniques.

The study of planetary interiors encompasses a wide area of research activity. At present the amount of available facts is far too limited to arrive at definite conclusions about the status quo and the evolutionary history of our planet. Experimental tools that provide information about candidate materials under high P–T conditions are invaluable in progressing with this task. In this paper, we have demonstrated how nuclear resonant scattering methods can contribute in the study of Earth materials, like iron and iron-bearing compounds. The assembly of a database of sound velocities, Grüneisen parameters, and electronic properties related to valence and spin state of Fe has just begun. Over the next decade, we anticipate a further increase in available x-ray intensity which will permit more accurate measurements. In addition, the synergy of nuclear resonant scattering methods with other x-ray techniques, e.g. x-ray diffraction for in-situ density determination, will be another crucial step toward improved data reliability in the high P–T sector.

This work was supported by the U.S. Department of Energy, Office of Science, Basic Energy Sciences, under Contract No. W-31-109-Eng-38.

References

- Akber-Knutson, S., G. Steinle-Neumann, and P. D. Asimow (2005), Effect of Al on the sharpness of the MgSiO_3 perovskite to post-perovskite phase transition, *Geophysical Research Letters*, *32*, doi:10.1029/2005GL023192.
- Alp, E. E., W. Sturhahn, and T. S. Toellner (2001), Lattice dynamics and inelastic nuclear resonance x-ray scattering, *J. Phys.: Condens. Matter*, *13*, 7645.
- Anderson, O. L. (1979), Evidence supporting the approximation $\gamma\rho = \text{const}$ for the Grüneisen parameter of the Earth’s lower mantle, *J. Geophys. Res.*, *81*, 3537–3542.

- Badro, J., G. Fiquet, F. Guyot, J. Rueff, V. V. Struzhkin, G. Vanko, and G. Monaco (2003), Iron partitioning in Earth’s mantle: Toward a deep lower mantle discontinuity, *Science*, *300*, 789–791.
- Badro, J., J. P. Rueff, G. Vanko, G. Monaco, G. Fiquet, and F. Guyot (2004), Electronic transitions in perovskite: Possible nonconvecting layers in the lower mantle, *Science*, *305*, 383–386.
- Bancroft, G. M., A. G. Maddock, and R. Burns (1967), Applications of the Mössbauer effect to silicate mineralogy - I. Iron silicates of known crystal structure, *Geochimica et Cosmochimica Acta*, *31*, 2219–2246.
- Barla, A., J. P. Sanchez, B. Malaman, B. P. Doyle, and R. Rüffer (2004a), Sm magnetism in the layered compound SmMn_2Ge_2 , *Phys. Rev. B*, *69*, 220,405, doi:10.1103/PhysRevB.69.220405.
- Barla, A., J.-P. Sanchez, A. Aksungur, R. L. J. Plessel, B. P. Doyle, R. Rüffer, and M. M. Abd-Elmeguid (2005a), Delocalization of the U 5f magnetic moments in $\text{U}(\text{In}_{0.6}\text{Sn}_{0.4})_3$ and UNiSn under high pressure, *J. Phys.: Condens. Matter*, *17*, S859–S870, doi:10.1088/0953-8984/17/11/015.
- Barla, A., et al. (2004b), Pressure-Induced Magnetic Order in Golden SmS , *Phys. Rev. Lett.*, *92*, 066,401, doi:10.1103/PhysRevLett.92.066401.
- Barla, A., et al. (2005b), Valence and magnetic instabilities in Sm compounds at high pressures, *J. Phys.: Condens. Matter*, *17*, S837–S848, doi:10.1088/0953-8984/17/11/013.
- Birch, F. (1952), Elasticity and constitution of the Earth’s interior, *Journal of Geophysical Research*, *57*, 227–286.
- Brown, J. M., and R. G. McQueen (1986), Phase transitions, Grüneisen parameter, and elasticity for shocked iron between 77 GPa and 400 GPa, *Journal of Geophysical Research*, *91*, 7485–7495.
- Chumakov, A. I., and W. Sturhahn (1999), Experimental aspects of inelastic nuclear resonant scattering, *Hyperfine Int.*, *123-124*, 781.
- Chumakov, A. I., R. Rüffer, H. Grünsteudel, H. F. Grünsteudel, G. Grübel, J. Metge, and H. A. Goodwin (1995), Energy Dependence of Nuclear Recoil Measured with Incoherent Nuclear Scattering of Synchrotron Radiation, *Europhys. Lett.*, *30*, 427.
- Dubrovinsky, L. S., S. K. Saxena, N. A. Dubrovinskaia, S. Rekhi, and T. L. Bihan (2000a), Grüneisen parameter of e-iron up to 300 GPa from in-situ x-ray study, *American Mineralogist*, *85*, 386–389.
- Dubrovinsky, L. S., S. K. Saxena, F. Tutti, S. Rekhi, and T. L. Bihan (2000b), In situ x-ray study of thermal expansion and phase transition of iron at multimegabar pressure, *Phys. Rev. Lett.*, *84*, 1720–1723.
- Dziewonski, A., and D. L. Anderson (1981), Preliminary reference Earth model, *Phys. Earth Planet. Inter.*, *25*, 297–356.
- Endres, G., F. Strokindl, H. Langhoff, and F. Gmelin (1981), Observation of Localized Modes in TbO_x and TbAl_2 by Resonance Absorption of γ -Quanta, *Z. Physik B*, *44*, 253.

- Fiquet, G., J. Badro, F. Guyot, H. Requardt, and M. Krisch (2001), Sound velocities in iron to 110 gigapascals, *Science*, *291*, 468–471.
- Frost, D. J., and F. Langenhorst (2002), The effect of Al₂O₃ on the Fe-Mg partitioning between magnesiowüstite and magnesium silicate perovskite, *Earth and Planetary Science Letters*, *199*, 227–241.
- Gaffney, E. S., and D. L. Anderson (1973), Effect of low-spin Fe²⁺ on the composition of the lower mantle, *J. Geophys. Res.*, *78*, 7005–7014.
- Gerdau, E., and H. de Waard (Eds.) (1999), *Nuclear Resonant Scattering of Synchrotron Radiation (Parts A&B)*, vol. Hyperfine Interact. 123-125, Baltzer Science Publishers.
- Gerdau, E., R. Rüffer, H. Winkler, W. Tolksdorf, C. P. Klages, and J. P. Hannon (1985), Nuclear Bragg Diffraction of Synchrotron Radiation in Yttrium Iron Garnet, *Phys. Rev. Lett.*, *54*(8), 835–838.
- Giefers, H., R. Lübbers, K. Rupprecht, G. Wortmann, D. Alfè, and A. I. Chumakov (2000), Phonon spectroscopy of oriented hcp iron, *High Press. Res.*, *22*, 501–506, doi:10.1080/08957950290011437.
- Grüneisen, E. (1926), *The state of a solid body, Handbook der Physik, vol.1*, Springer-Verlag.
- Hearmon, R. F. S. (1984), *The elastic constants of crystals and other anisotropic materials*, 559 pp., Springer-Verlag.
- Hemley, R. J., H.-K. Mao, and V. V. Struzhkin (2005), Synchrotron radiation and high pressure: new light on materials under extreme conditions, *J. Synchrotron Rad.*, *12*, 135–154, doi:10.1107/S0909049504034417.
- Hirose, K., Y. Fei, Y. Ma, and H. K. Mao (1999), The fate of subducted basaltic crust in the Earth’s lower mantle, *Nature*, *397*, 53–56.
- Hu, M. Y., W. Sturhahn, T. S. Toellner, P. Hession, J. Sutter, and E. E. Alp (1999), Data analysis for inelastic nuclear resonant absorption experiments with synchrotron radiation, *Nucl. Instrum. Methods A*, *428*, 551.
- Hu, M. Y., W. Sturhahn, T. S. Toellner, P. D. Mannheim, D. E. Brown, J. Zhao, and E. E. Alp (2003), Measuring velocity of sound with nuclear resonant inelastic x-ray scattering, *Phys. Rev. B*, *67*, 094,304, doi:10.1103/PhysRevB.67.094304.
- Irifune, T. (1994), Absence of an aluminum phase in the upper part of the Earth’s lower mantle, *Nature*, *370*, 131–133.
- Ishii, M., and J. Tromp (1999), Normal-mode and free-air gravity constraints on lateral variations in velocity and density of the Earth’s mantle, *Science*, *285*, 1231–1236.
- Jackson, I., and S. K. Khanna (1990), Shear-mode softening and high pressure polymorphism of wüstite (Fe_{1-x}O), *Journal of Geophysical Research*, *95*, 21,671–21,685.
- Jackson, J. M., W. Sturhahn, G. Shen, J. Zhao, M. Y. Hu, D. Errandonea, J. D. Bass, and Y. Fei (2005), A synchrotron Mössbauer spectroscopy study of (Mg,Fe)SiO₃ perovskite up to 120 GPa, *American Mineralogist*, *90*, 199, doi:10.2138/am.2005.1633.

- Jacobsen, S. D., H. J. Reichmann, H. A. Spetzler, S. J. Mackwell, J. R. Smyth, R. J. Angel, and C. A. McCammon (2002), Structure and elasticity of single-crystal (Mg,Fe)O and a new method of generating shear waves for gigahertz interferometry, *Journal of Geophysical Research*, *107*, doi:10.1029/2001JB000490.
- Jacobsen, S. D., H. Spetzler, H. J. Reichmann, and J. R. Smith (2004), Shear waves in the diamond-anvil cell reveal pressure-induced instability in (Mg,Fe)O, *Proceedings of the National Academy of Science*, *101*, 5867–5871.
- Jeanloz, R. (1979), Properties of iron at high pressure and the state of the core, *Journal of Geophysical Research*, *84*, 6059–6069.
- Karki, B. B., and J. Crain (1998), First-principles determination of elastic properties of CaSiO₃ perovskite at lower mantle pressures, *Geophysical Research Letters*, *25*, 2741–2744.
- Kellogg, L. H., B. H. Hager, and R. D. van der Hilst (1999), Compositional stratification in the deep mantle, *Science*, *283*, 1881–1884.
- Kesson, S. E., J. D. F. Gerald, J. M. G. Shelley, and R. L. Whithers (1995), Phase relations, structure and crystal chemistry of some aluminous silicate perovskites, *Earth and Planetary Science Letters*, *134*, 187–201.
- Kiefer, B., L. Stixrude, and R. Wentzcovitch (2002), Elasticity of (Mg,Fe)SiO₃-perovskite at high-pressures, *Geophysical Research Letters*, *29*, doi:10.1029/2002GL014683.
- Kobayashi, H., T. Kamimura, D. Alfè, W. Sturhahn, J. Zhao, and E. E. Alp (2004), Phonon density of states and compression behavior in iron sulfide under pressure, *Phys. Rev. Lett.*, *93*, 195503, doi:10.1103/PhysRevLett.93.195503.
- Kohn, V. G., A. I. Chumakov, and R. Rüffer (1998), Nuclear resonant inelastic absorption of synchrotron radiation in an anisotropic single crystal, *Phys. Rev. B*, *58*, 8437.
- Kung, J., B. Li, D. J. Weidner, J. Zhang, and R. J. Liebermann (2002), Elasticity of (Mg_{0.83}Fe_{0.17})O ferropericlasite at high pressure: ultrasonic measurements in conjunction with x-radiation techniques, *Earth and Planet. Sci. Lett.*, *203*, 557–566.
- Lengsdorf, R., A. Barla, J. A. Alonso, M. J. Martinez-Lope, H. Micklitz, and M. M. Abd-Elmeguid (2004), The observation of the insulator metal transition in EuNiO₃ under high pressure, *J. Phys.: Condens. Matter*, *16*, 3355–3360, doi:10.1088/0953-8984/16/20/006.
- Li, J., et al. (2004), Electronic spin state of iron in lower mantle perovskite, *Proceedings of the National Academy of Sciences*, *101*, 14,027–14,030, doi:10.1073/pnas.0405804101.
- Liebermann, R. C., and E. Schreiber (1968), Elastic constants of polycrystalline hematite as a function of pressure to 3 kilobars, *Journal of Geophysical Research*, *73*, 6585–6590.
- Lin, J. F., Y. Fei, W. Sturhahn, J. Zhao, H. K. Mao, and R. J. Hemley (2004a), Magnetic transition and sound velocities of Fe₃S at high pressure: implications for Earth and planetary cores, *Earth Planet. Sci. Lett.*, *226*, 33, doi:10.1016/j.epsl.2004.07.018.
- Lin, J. F., W. Sturhahn, J. Zhao, G. Shen, H. K. Mao, and R. J. Hemley (2004b), Absolute temperature measurement in a laser-heated diamond anvil cell, *Geophys. Res. Lett.*, *31*, L14,611, doi:10.1029/2003GL020599.

- Lin, J. F., V. V. Struzhkin, S. D. Jacobsen, M. Y. Hu, P. Chow, J. Kung, H. Liu, H. K. Mao, and R. J. Hemley (2005), Spin transition of iron in magnesiowüstite in the Earth's lower mantle, *Nature*, *436*, 377–380, doi:10.1038/nature03825.
- Lin, J. F., et al. (2003), Sound velocities of iron-nickel and iron-silicon alloys at high pressures, *Geophys. Res. Lett.*, *30*, 2112, doi:10.1029/2003GL018405.
- Lübbbers, R., M. Pleines, H.-J. Hesse, G. Wortmann, H. F. Grünsteudel, R. Rüffer, O. Leupold, and J. Zukrowski (1999a), Magnetism under high pressure studied by ^{57}Fe and ^{151}Eu nuclear scattering of synchrotron radiation, *Hyperfine Interact.*, *120/121*, 49–58.
- Lübbbers, R., G. Wortmann, and H. F. Grünsteudel (1999b), High-pressure studies with nuclear scattering of synchrotron radiation, *Hyperfine Interact.*, *123/124*, 529.
- Lübbbers, R., H. F. Grünsteudel, A. I. Chumakov, and G. Wortmann (2000a), Density of Phonon States in Iron at High Pressure, *Science*, *287*, 1250–1253.
- Lübbbers, R., K. Rupprecht, and G. Wortmann (2000b), High-pressure Mössbauer studies of magnetism in RFe_2 Laves phases and Eu-chalcogenides, *Hyperfine Interact.*, *128*, 115–135.
- Machova, A., and S. Kadeckova (1977), Elastic constants of iron-silicon alloy single crystals, *Czech. Journal of Physics*, *B27*, 555–563.
- Mao, H. K., et al. (2001), Phonon density of states of iron up to 153 Gigapascals, *Science*, *292*, 914.
- Mao, W. L., G. Shen, V. B. Prakapenka, Y. Meng, A. J. Campbell, D. L. Heinz, J. Shu, R. J. Hemley, and H. K. Mao (2004), Ferromagnesium postperovskite silicates in the D'' later of the Earth, *Proceedings of the National Academy of Sciences*, *101*, 15,866–15,869.
- McCammon, C. A. (1997), Perovskite as a possible sink for ferric iron in the lower mantle, *Nature*, *387*, 694–696.
- Merkel, S., A. F. Goncharov, H. K. Mao, P. Gillet, and R. J. Hemley (2000), Raman spectroscopy of iron to 152 gigapascals: Implications for Earth's inner core, *Science*, *288*, 1626–1629.
- Murakami, M., K. Hirose, K. Kawamura, N. Sata, and Y. Onishi (2004), Post-perovskite phase transition in MgSiO_3 , *Science*, *304*, 855–858.
- Nasu, S. (1994), High pressure studies with nuclear resonant scattering, *Hyperfine Interact.*, *90*, 59.
- Nasu, S. (1998), High pressure experiments with synchrotron radiation, *Hyperfine Interact.*, *113*, 97.
- Papandrew, A. B., A. F. Yue, B. Fultz, I. Halevy, W. Sturhahn, T. S. Toellner, E. E. Alp, and H.-k.Mao (2004), Vibrational modes in nanocrystalline iron under high pressure, *Phys. Rev. B*, *69*, 144,301, doi:10.1103/PhysRevB.69.144301.
- Pleines, M., R. Lübbbers, M. Strecker, G. Wortmann, O. Leupold, Y. V. Shvyd'ko, E. Gerdau, and J. Metge (1999), Pressure-induced valence transition in EuNi_2Ge_2 studied by ^{151}Eu nuclear forward scattering of synchrotron radiation, *Hyperfine Interact.*, *120/121*, 181.

- Rai, B. K., S. M. Durbin, E. W. Prohofsky, J. T. Sage, M. K. Ellison, W. R. Scheidt, W. Sturhahn, and E. E. Alp (2002), Iron normal mode dynamics in a porphyrin-imidazole model for deoxyheme proteins, *Phys. Rev. E*, *66*, 051,904, doi:10.1103/PhysRevE.66.051904.
- Rupprecht, K., T. Friedmann, H. Giefers, G. Wortmann, B. Doyle, and J. Zukrowski (2000), High-pressure/high-temperature NFS study of magnetism in LuFe_2 and ScFe_2 , *High Press. Res.*, *22*, 189–194, doi:10.1080/08957950290010636.
- Scheidt, W. R., S. M. Durbin, and J. T. Sage (2005), Nuclear resonance vibrational spectroscopy - NRVS, *J. Inorg. Biochem.*, *99*, 60–71, doi:10.1016/j.jinorgbio.2004.11.004.
- Seto, M., Y. Yoda, S. Kikuta, X. Zhang, and M. Ando (1995), Observation of Nuclear Resonant Scattering Accompanied by Phonon Excitation Using Synchrotron Radiation, *Phys. Rev. Lett.*, *74*, 3828.
- Shannon, R. D., and C. T. Prewitt (1969), Effective ionic radii in oxides and fluorides, *Acta Cryst.*, *B25*, 925–946.
- Shen, G., W. Sturhahn, E. E. Alp, J. Zhao, T. S. Toellner, V. B. Prakapenka, Y. Meng, and H.-K. Mao (2004), Phonon density of states in iron at high pressures and high temperatures, *Phys. Chem. Minerals*, *31*, 353, doi:10.1007/s00269-004-0403-l.
- Sherman, D. M. (1988), High-spin to low-spin transition of iron(II) oxides at high pressures: possible effects on the physics and chemistry of the lower mantle, in *Structural and magnetic phase transitions in minerals*, edited by S. Ghose, J. M. D. Coey, and E. Salje, pp. 113–128, Springer Verlag, New York.
- Sherman, D. M. (1991), The high-pressure electronic structure of magnesiowustite (Mg,Fe)O: applications to the physics and chemistry of the lower mantle, *J. Geophys. Res.*, *96*, 14,299–14,312.
- Sherman, D. M., and H. J. F. Jansen (1995), First-principle prediction of the high-pressure phase transition and electronic structure of FeO : implications for the chemistry of the lower mantle and core, *Geophys. Res. Lett.*, *22*, 1001–1004.
- Singwi, K. S., and A. Sjölander (1960), Resonance Absorption of Nuclear Gamma Rays and the Dynamics of Atomic Motions, *Phys. Rev.*, *120*, 1093.
- Sinogeikin, S. V., J. Zhang, and J. D. Bass (2004), Elasticity of single crystal and polycrystalline MgSiO_3 perovskite by Brillouin spectroscopy, *Geophysical Research Letters*, *31*, L06,620, doi:10.1029/2004GL019559.
- Struzhkin, V. V., et al. (2001), Nuclear inelastic x-ray scattering of FeO to 48 GPa, *Phys. Rev. Lett.*, *87*, 255,501, doi:10.1103/PhysRevLett.87.255501.
- Sturhahn, W. (2000), CONUSS and PHOENIX: Evaluation of nuclear resonant scattering data, *Hyperfine Int.*, *125*, 149.
- Sturhahn, W. (2001), Phase problem in synchrotron Mössbauer spectroscopy, *Phys. Rev. B*, *63*, 94,105, doi:10.1103/PhysRevB.63.094105.
- Sturhahn, W. (2004), Nuclear resonant spectroscopy, *J. Phys.: Condens. Matter*, *16*, S497–S530, doi:10.1088/0953-8984/16/5/009.

- Sturhahn, W., and A. I. Chumakov (1999), Lamb-Mössbauer factor and second-order Doppler shift from inelastic nuclear resonant absorption, *Hyperfine Int.*, 123-124, 809.
- Sturhahn, W., and V. Kohn (1999), Theoretical aspects of inelastic nuclear resonant scattering, *Hyperfine Int.*, 123-124, 367.
- Sturhahn, W., E. E. Alp, T. S. Toellner, P. Hession, M. Hu, and J. Sutter (1998), Introduction to nuclear resonant scattering with synchrotron radiation, *Hyperfine Int.*, 113, 47.
- Sturhahn, W., C. L'abbé, and T. S. Toellner (2004), Exo-interferometric phase determination in nuclear resonant scattering, *Europhys. Lett.*, 66, 506, doi:10.1209/epl/i2003-10235-7.
- Sturhahn, W., J. M. Jackson, and J. F. Lin (2005), The spin state of lower mantle minerals in Earth's lower mantle, *Geophysical Research Letters*, 32, L12,307, doi:10.1029/2005GL022802.
- Sturhahn, W., et al. (1995), Phonon density of states measured by inelastic nuclear resonant scattering, *Phys. Rev. Lett.*, 74, 3832.
- Toellner, T. (2000), Monochromatization of synchrotron radiation for nuclear resonant scattering experiments, *Hyperfine Interactions*, 125, 3–28.
- Toellner, T. S., M. Y. Hu, W. Sturhahn, G. Bortel, E. E. Alp, and J. Zhao (2001), Crystal monochromator with a resolution beyond 10^8 , *J. Synchrotron Rad.*, 8, 1082.
- Trampert, J., F. Deschamps, J. Resovski, and D. Yuen (2004), Probabilistic tomography maps chemical heterogeneities throughout the lower mantle, *Science*, 306, 853–856.
- van der Hilst, R. D., and H. Kårason (1999), Compositional heterogeneity in the bottom 1000 kilometers of Earth's mantle: Toward a hybrid convection model, *Science*, 283, 1885–1888.
- Visscher, W. M. (1960), Study of lattice vibrations by resonance absorption of nuclear gamma rays, *Annals of Phys.*, 9, 194–210.
- Weast, R. C. (1984), *CRC Handbook of Chemistry and Physics*, 65th edition, CRC Press, Boca Raton, FL.
- Weiss, H., and H. Langhoff (1979), Observation of Localized Modes in TbO_x using the Mößbauer Effect, *Z. Physik B*, 33, 365.
- Wood, B. J., and D. C. Rubie (1996), The effect of alumina on phase transformations at the 660-kilometer discontinuity from Fe-Mg partitioning experiments, *Science*, 273, 1522–1524.
- Wortmann, G., K. Rupprecht, and H. Giefers (2002), High-Pressure Studies of Magnetism and Lattice Dynamics by Nuclear Resonant Scattering of Synchrotron Radiation, *Hyperfine Interact.*, 144/145, 103–117.
- Zhang, L., J. Stanek, S. S. Hafner, H. Ahsbahs, H. F. Grünsteudel, J. Metge, and R. Rüffer (1999), ^{57}Fe nuclear forward scattering of synchrotron radiation in hedenbergite $\text{CaFeSi}_2\text{O}_6$ at hydrostatic pressures up to 68 GPa, *American Mineralogist*, 84, 447.
- Zhao, J., W. Sturhahn, J.-F. Lin, G. Shen, E. E. Alp, and H.-K. Mao (2004), Nuclear Resonant Scattering at High Pressure and High Temperature, *High Pressure Research*, 24, 447–457, doi:10.1080/08957950412331331727.

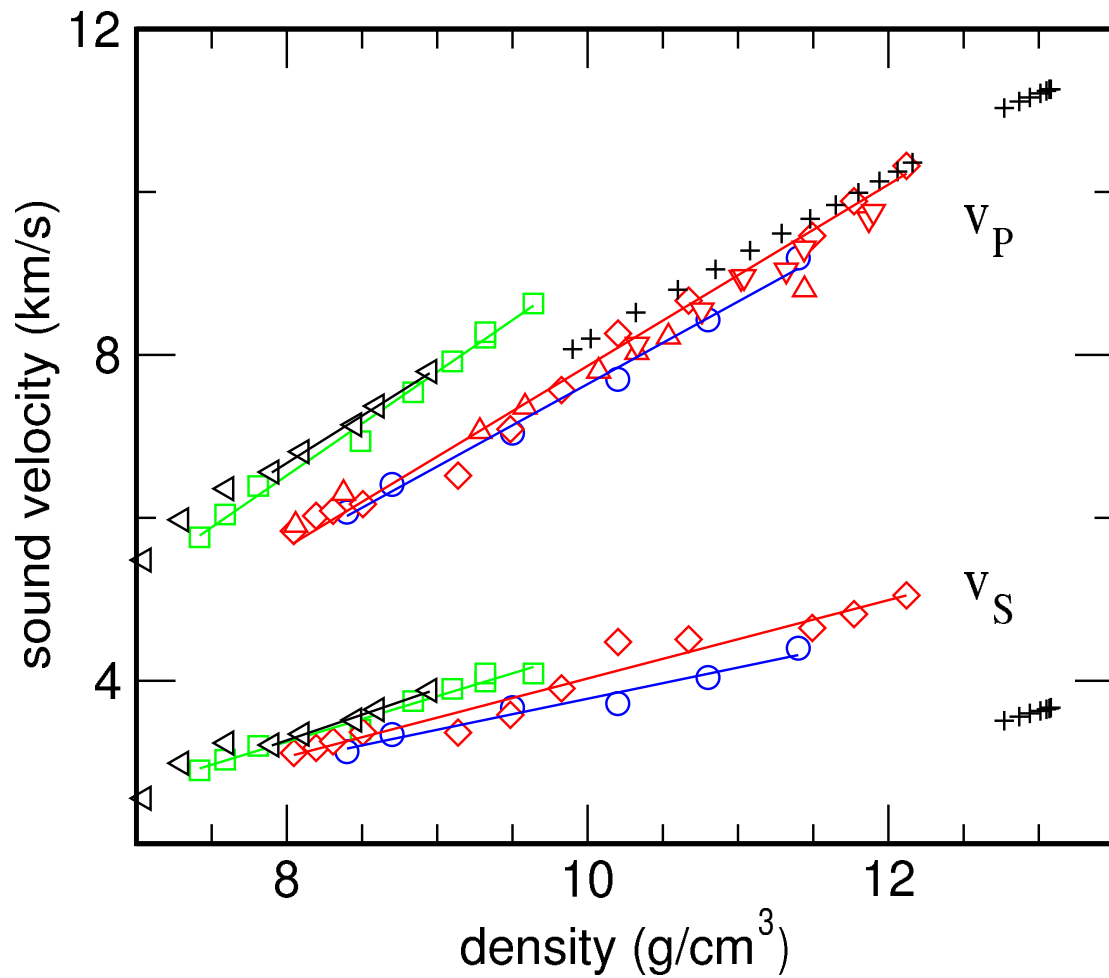


Figure 5: Compressional wave and shear wave velocities versus density. Results from NRIXS data: diamonds, Fe (*Mao et al.*, 2001); circles, $\text{Fe}_{0.92}\text{Ni}_{0.08}$ and rectangles, $\text{Fe}_{0.85}\text{Si}_{0.15}$ (*Lin et al.*, 2003); left triangles, Fe_3S (*Lin et al.*, 2004a). Other results: triangles up, Fe, IXS (*Fiquet et al.*, 2001); triangles down, Fe, shock-wave (*Brown and McQueen*, 1986); crosses, PREM (*Dziewonski and Anderson*, 1981). The straight lines are fits to the NRIXS results and suggest the validity of Birch's law.

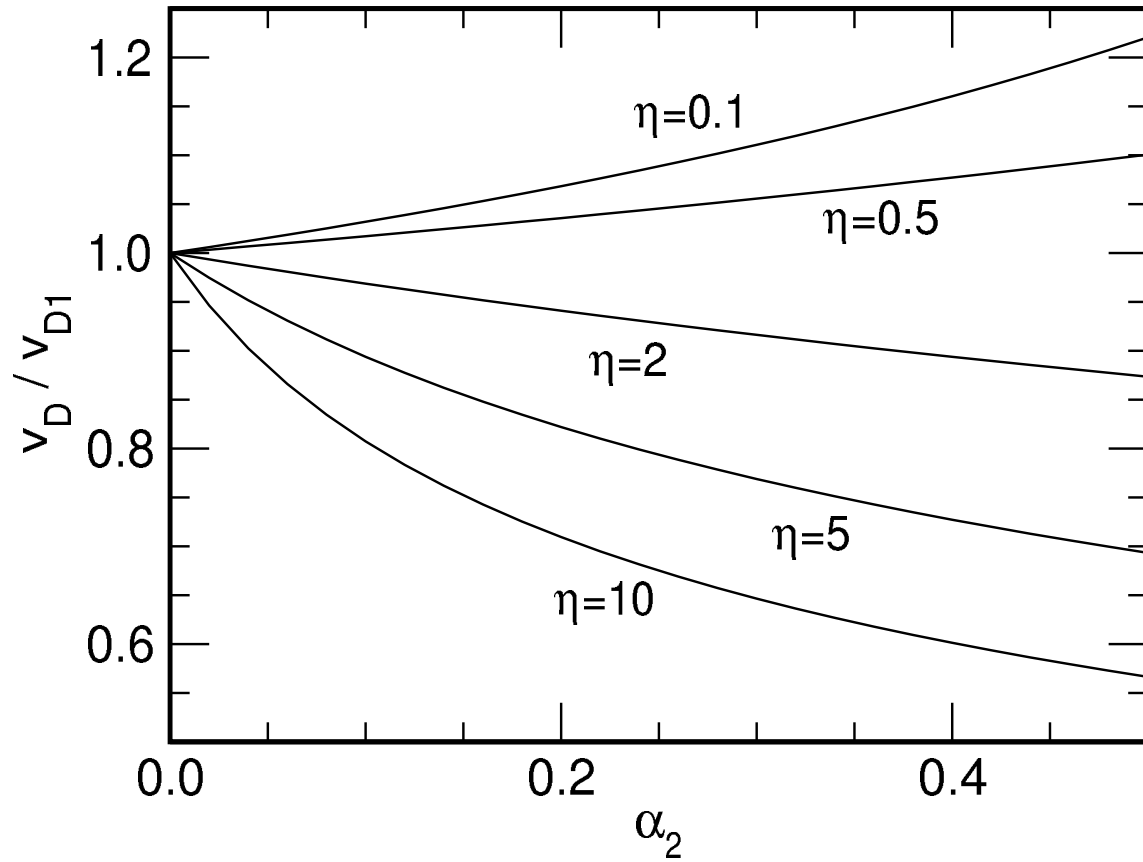


Figure 6: Correction of the measured Debye sound velocity in mixed compounds versus the concentration of the contaminant. (17) was used with the specified values for $\eta = (\rho_2 v_{D1}^3)/(\rho_1 v_{D2}^3)$. Large η describe the admixture of a contaminant with high density and/or low Debye sound velocity.

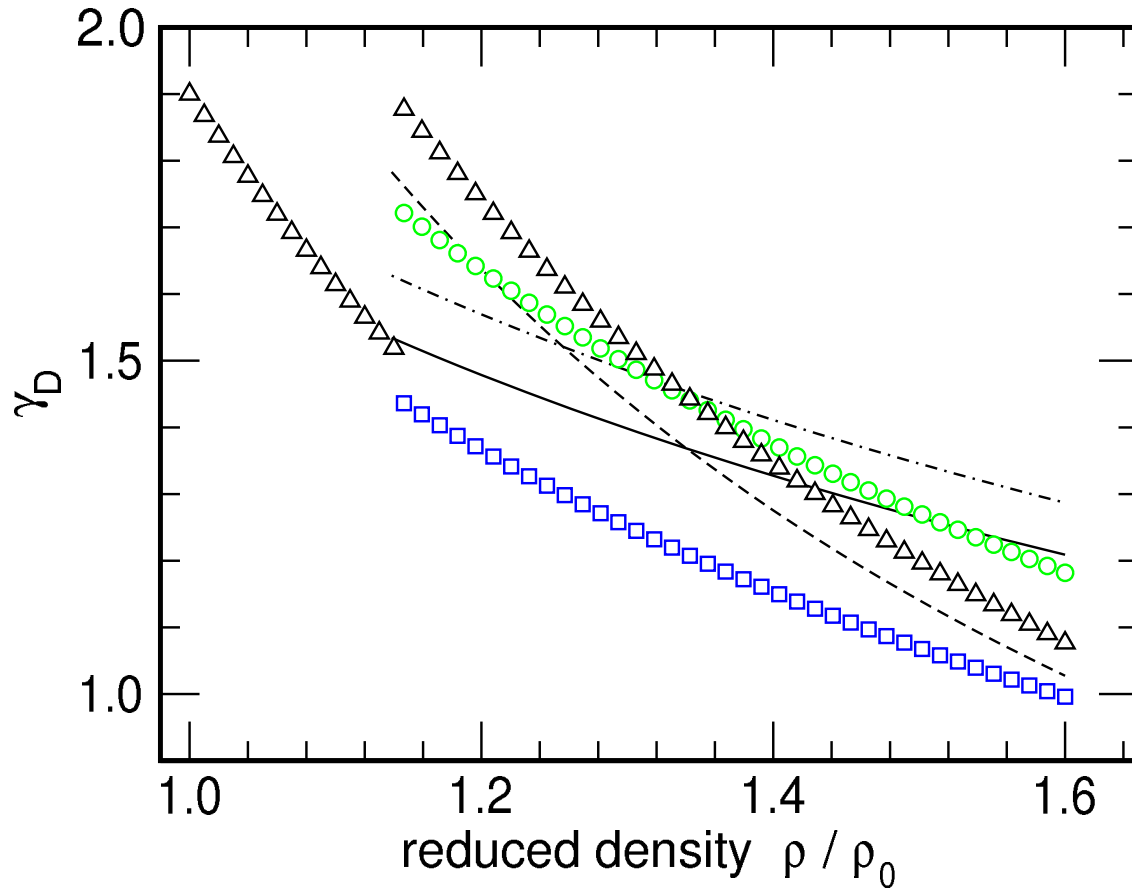


Figure 7: Debye-Grüneisen parameter versus reduced density. Results derived from NRIXS data: triangles, Fe (*Mao et al.*, 2001); rectangles, $\text{Fe}_{0.92}\text{Ni}_{0.08}$ and circles, $\text{Fe}_{0.85}\text{Si}_{0.15}$ (*Lin et al.*, 2003). For comparison, hcp-Fe: solid line, Raman spectroscopy (*Merkel et al.*, 2000); dashed line, shock compression (*Jeanloz*, 1979); dashed-dotted line, XRD (*Dubrovinsky et al.*, 2000a,b).

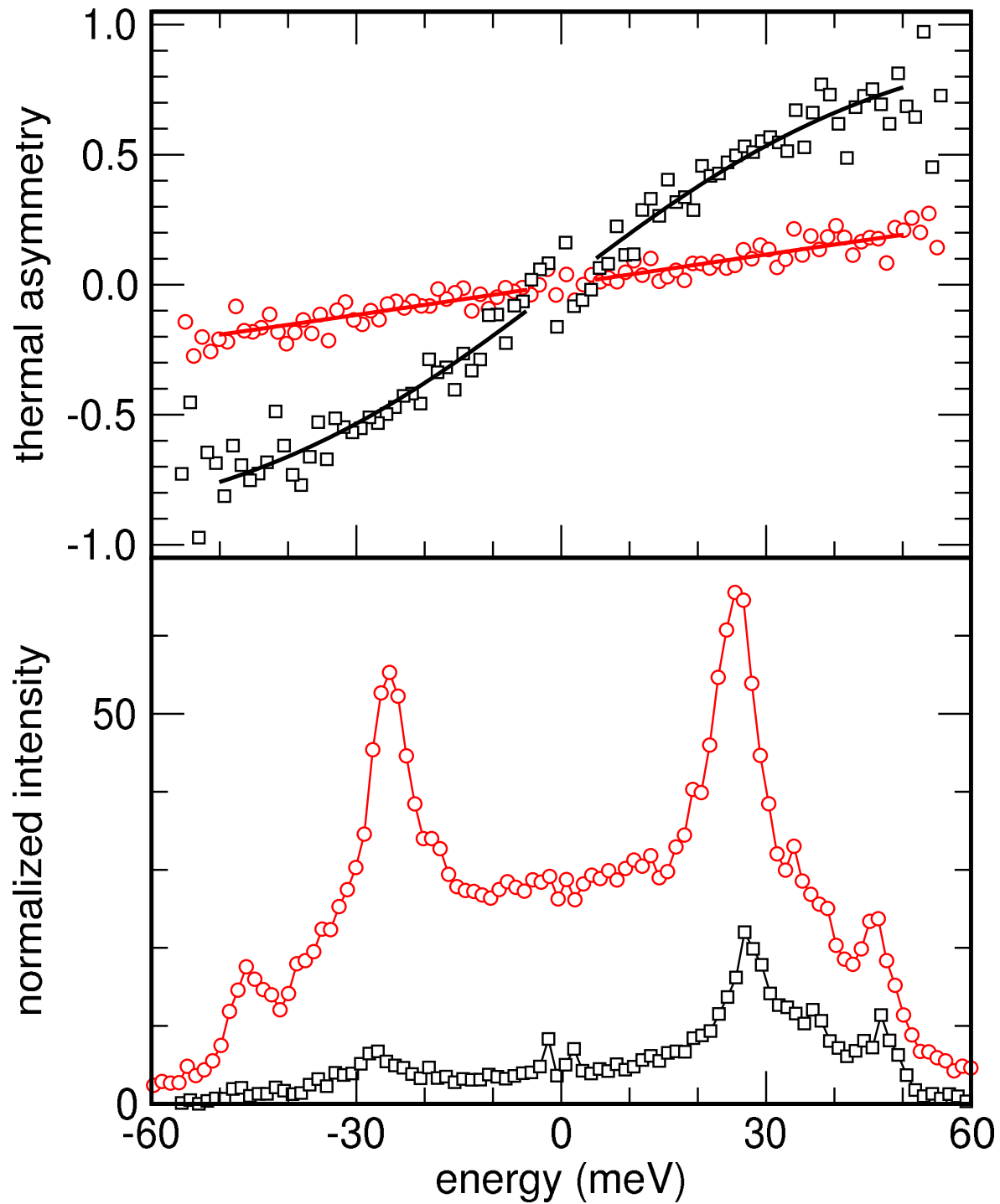


Figure 8: The effect of the detailed balance rule on NRIXS data. Bottom graph: normalized intensity for hcp-iron at 50 GPa and ambient temperature (squares) and at 55 GPa and 1500 K (circles) (*Lin et al., 2004b*). The elastic peak has been subtracted. Top graph: thermal asymmetry calculated according to Eq.22 with solid lines corresponding to fits with temperatures of 293(15) K and 1500(100) K.

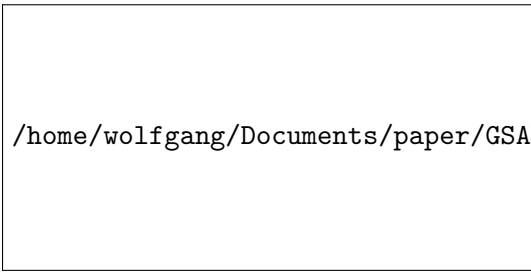


Figure 9: Temperatures determined by spectroradiometric method and from NRIXS data. The iron sample was mounted inside a diamond anvil cell and pressurized to about 58 GPa (*Lin et al.*, 2004b). The red symbol at 1500 K indicates the temperature determined from the high-temperature spectrum in Figure 8 on page 27. The straight line indicates identical temperatures.

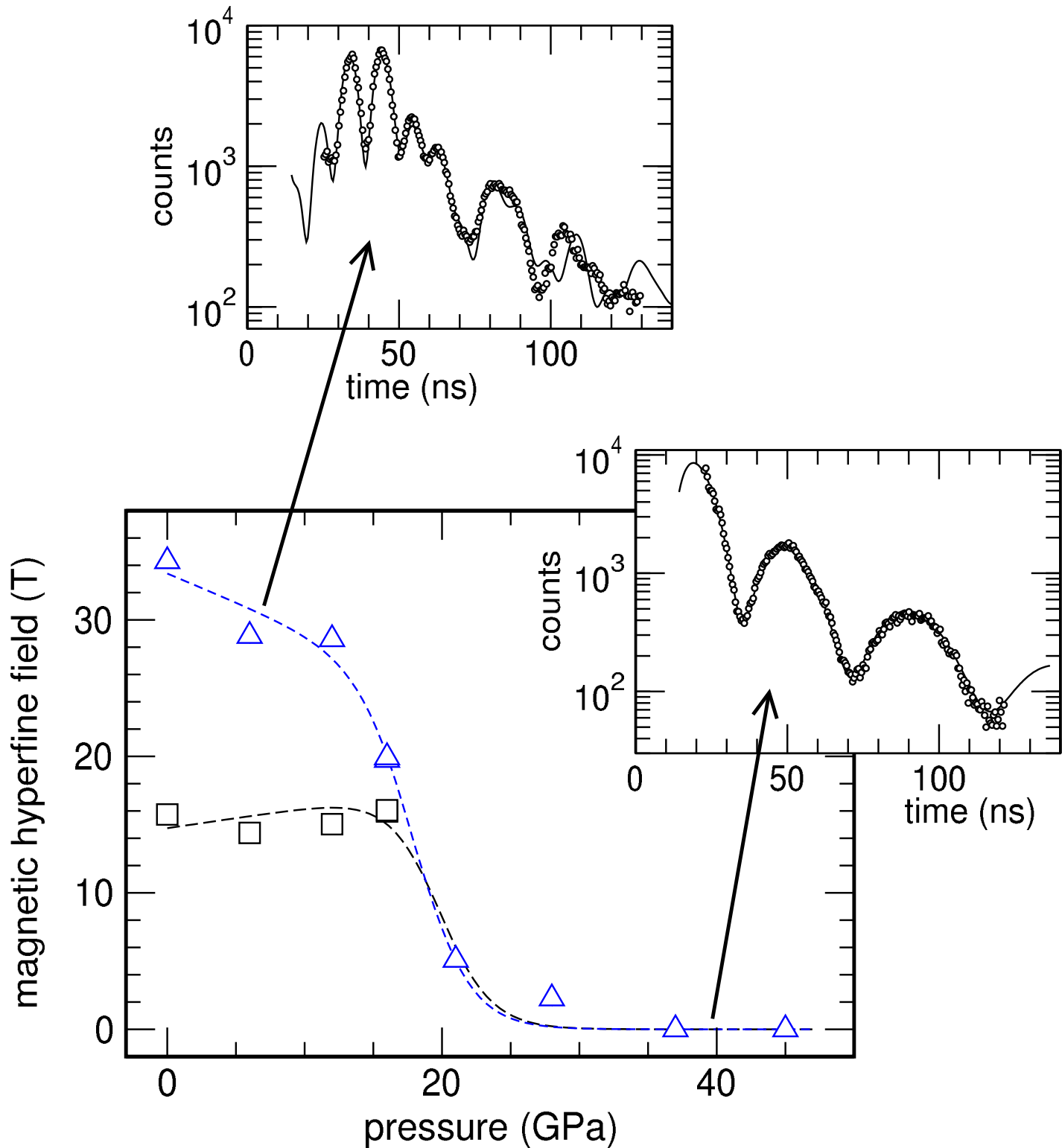


Figure 10: Magnetic hyperfine fields and normalized sound velocities of Fe_3S with increasing pressure and time spectra recorded at 6 GPa and at 45 GPa. Below about 20 GPa, the low-pressure magnetic phase displays two magnetic field sites. The higher magnetic field (triangles) decreases with increasing pressure, whereas the lower magnetic field (squares) remains almost constant. A magnetic collapse occurs at approximately 21 GPa. The dashed lines are guides to the eye. The magnetic collapse is accompanied by a change in the pressure dependence of the normalized compressional (diamonds) and shear (circles) wave velocities as shown in the lower panel. At low pressure, the fast oscillations in the time spectrum clearly indicate the magnetic nuclear level splitting. At high pressure the oscillations are significantly slower and result from a remaining quadrupole splitting and the rather large thickness of the sample.

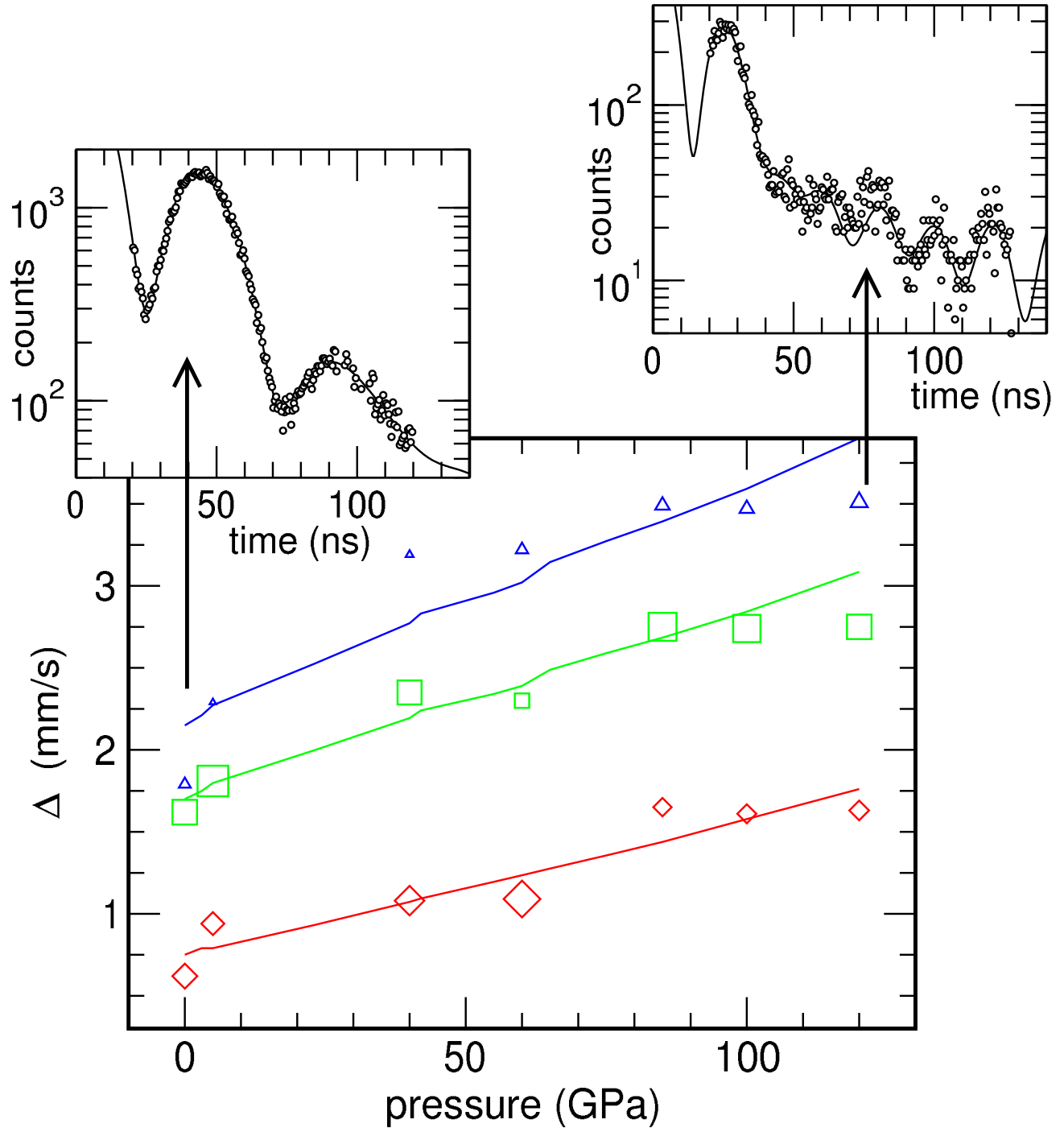


Figure 11: Quadrupole splittings (Δ) of the three Fe sites in $\text{Mg}_{0.95}\text{Fe}_{0.05}\text{SiO}_3$ versus pressure, isomer shifts (δ) between Fe^{2+} and Fe^{3+} sites, and time spectra recorded at ambient pressure and at 120 GPa. The solid lines are calculated using an isomorphic volume reduction of the unit cell (*Jackson et al.*, 2005). In the top panel, triangles and rectangles: sites associated with Fe^{2+} ; diamonds: Fe^{3+} site. The symbol size is proportional to the weight of the corresponding Fe site. In the lower panel, triangles: $\text{Mg}_{0.9}\text{Fe}_{0.1}\text{SiO}_3$, diamonds: $\text{Mg}_{0.95}\text{Fe}_{0.05}\text{SiO}_3$. Above about 70 GPa the isomer shift between Fe^{2+} and Fe^{3+} sites changes little. At low pressure, the slower oscillations in the time spectrum clearly indicate smaller nuclear level splittings for all sites. The time spectra were evaluated with the CONUSS programs to provide quadrupole splittings, weights, and isomer shifts of each Fe site (*Sturhahn*, 2000). Circles: experimental time spectra; solid lines: best calculated time spectra. The data are taken from *Jackson et al.* 2005.